IOP Publishing Electron. Struct. 6 (2024) 033002 https://doi.org/10.1088/2516-1075/ad5898

Electronic Structure

TOPICAL REVIEW

Halide perovskites from first principles: from fundamental optoelectronic properties to the impact of structural and chemical heterogeneity

Marina R Filip[1,*] and Linn Leppert[2,*]

[1] Department of Physics, University of Oxford, Oxford, United Kingdom
[2] MESA+ Institute for Nanotechnology, University of Twente, 7500 AE Enschede, The Netherlands
* Authors to whom any correspondence should be addressed.

E-mail: marina.filip@physics.ox.ac.uk and l.leppert@utwente.nl

Keywords: halide perovskites, first-principles calculations, density functional theory, many-body perturbation theory, optoelectronic properties, excitons

OPEN ACCESS

RECEIVED
12 February 2024

REVISED
10 April 2024

ACCEPTED FOR PUBLICATION
14 June 2024

PUBLISHED
22 July 2024

Abstract

Organic-inorganic metal-halide perovskite semiconductors have outstanding and widely tunable optoelectronic properties suited for a broad variety of applications. First-principles numerical modelling techniques are playing a key role in unravelling structure-property relationships of this structurally and chemically diverse family of materials, and for predicting new materials and properties. Herein we review first-principles calculations of the photophysics of halide perovskites with a focus on the band structures, optical absorption spectra and excitons, and the effects of electron- and exciton-phonon coupling and temperature on these properties. We focus on first-principles approaches based on density functional theory and Green's function-based many-body perturbation theory and provide an overview of these approaches. While a large proportion of first-principles studies have been focusing on the prototypical ABX_3 single perovskites based on Pb and Sn, recent years have witnessed significant efforts to further functionalize halide perovskites, broadening this family of materials to include double perovskites, quasi-low-dimensional structures, and other organic-inorganic materials, interfaces and heterostructures. While this enormous chemical space of perovskite and perovskite-like materials has only begun to be tapped experimentally, recent advances in theoretical and computational methods, as well as in computing infrastructure, have led to the possibility of understanding the photophysics of ever more complex systems. We illustrate this progress in our review by summarizing representative studies of first-principles calculations of halide perovskites with various degrees of complexity.

1. Introduction

Organic-inorganic metal-halide perovskites (halide perovskites in the following) have swept to the forefronts of energy research in the past decade due to their record-breaking optoelectronic performance and unique combination of properties, including large absorption coefficients [1], a widely tunable electronic structure [2], mixed ionic-electronic conductivity [3], a soft lattice [4–6], and optoelectronic properties which are largely resilient to defects [7, 8]. The chemical and structural diversity of this material class with thousands of stable compounds has led to a wide range of applications; a non-exhaustive list of examples includes photovoltaics [9, 10], lighting [11, 12], and detectors [13, 14] as well as electrocatalysis [15] and next-generation space-flight [16]. While many halide perovskites are all-inorganic materials, the conception of hybrid organic-inorganic perovskites has paved new ways for material synthesis, functionalization, and applications. Furthermore, the field has seen an unprecedented feedback loop between materials discovery and application. Not only have new perovskite and perovskite-inspired materials been synthesised for the

first time in recent years, but also many materials known (and somewhat overlooked) for decades, have been re-discovered and implemented in devices [17, 18].

First-principles calculations play a central role in unravelling fundamental structure-property relationships of halide perovskites, as well as predicting new materials and emerging properties. Hybrid halide perovskites pose unique challenges to numerical modelling techniques because of the intricate dynamical interactions between their organic and inorganic sublattices and resulting multiscale phenomenology that governs their properties. Most hybrid and all-inorganic halide perovskites of interest exhibit strong spin–orbit interactions, electron correlation, as well as electron- and exciton-phonon interactions. As a consequence, halide perovskites have become important testbeds for existing methods and drivers of new first-principles method development.

The aim of this review article is to provide an overview of the most popular first-principles methods used to study halide perovskites and review representative results emerging therefrom. This review does not aim to provide an exhaustive survey of either the first-principles methods or the halide perovskites literature. Instead, we wish to survey the research directions in which first-principles methods have had, in our view, their most impactful contributions, and to provide a basic overview of these computational frameworks. Our goal is to aid interested readers in better understanding both the challenges overcome by past studies and identifying opportunities for future developments. All material classes relevant for this article are going to be described in section 2. We will focus on results obtained from density functional theory (DFT) and Green's function-based many-body perturbation theory (MBPT). These methods will be introduced in section 3 with references to more comprehensive reviews for readers interested in more detailed discussions of the fundamentals and recent developments in DFT and Green's function-based MBPT. In section 4 we review the fundamental optoelectronic properties of single perovskites with chemical formula ABX_3, including a survey of recent calculations of electronic and optical excitations and charge-carrier transport properties. In section 5 we will provide insights into the impact of chemical and structural heterogeneity on optoelectronic properties. This includes calculations on both single ABX_3 perovskites with mixed A, B, and X sites, but also on chemically and structurally more complex perovskite and perovskite-inspired materials, including the quaternary double perovskites and quasi-low-dimensional materials in which optoelectronic properties are governed by quantum and dielectric confinement. Finally in section 6, we give our perspective on the most pressing challenges for future first-principles studies of halide perovskites and our conclusions.

2. Structural and chemical classification of perovskites

Halide perovskites are a vast class of structurally and compositionally diverse crystalline materials that have been known since the 19th century. They consist of anionic metal-halide octahedra connected through their corners in three, two, one or zero dimensions and charge-compensated by inorganic or organic cations. Contrary to the structurally related oxide perovskites that have been studied intensely for decades for their ferroelectric, superconducting, magnetic, multiferroic, and other emerging properties [19–21], halide perovskites only recently received a surge of interest, primarily because of the outstanding photovoltaic efficiency of the organic-inorganic halide perovskite $CH_3NH_3PbI_3$. In the following, we give an overview of the most important perovskite (-inspired) material classes covered in this review, diverging from a strict definition of ABX_3 perovskites. We focus entirely on halide perovskites, in which the X site is a halogen anion, i.e. I^-, Br^-, Cl^-, or more rarely F^-.

2.1. Single perovskites

Single halide perovskites, schematically shown in figure 1(a), are 3D solids with chemical formula ABX_3, where the B site is occupied by a divalent cation such as Pb^{2+} or Sn^{2+}. The cuboctahedral cavity spanned by the corner-sharing metal-halide octahedra fits an inorganic cation such as Cs^+ or small molecular cations such as methylammonium ($CH_3NH_3^+$ = MA) or formamidinium ($CH(NH_2)_2^+$ = FA). The structural stability of single perovskites is usually discussed in terms of Goldschmidt's tolerance factor [22]. This is a packing argument that allows to predict whether certain combinations of A, B, and X site ions will form a 3D perovskite or prefer other structural motifs, and can be extended to organic-inorganic perovskites [23]. Similar to oxide perovskites, halide perovskites have a complex potential energy landscape, and typically feature several structural phases as a function of temperature, pressure, strain, and chemical composition. The most common energy-lowering structural distortion in halide perovskites is octahedral tilting; for example, the typical orthorhombic structure that many lead halide perovskites arrange in at low

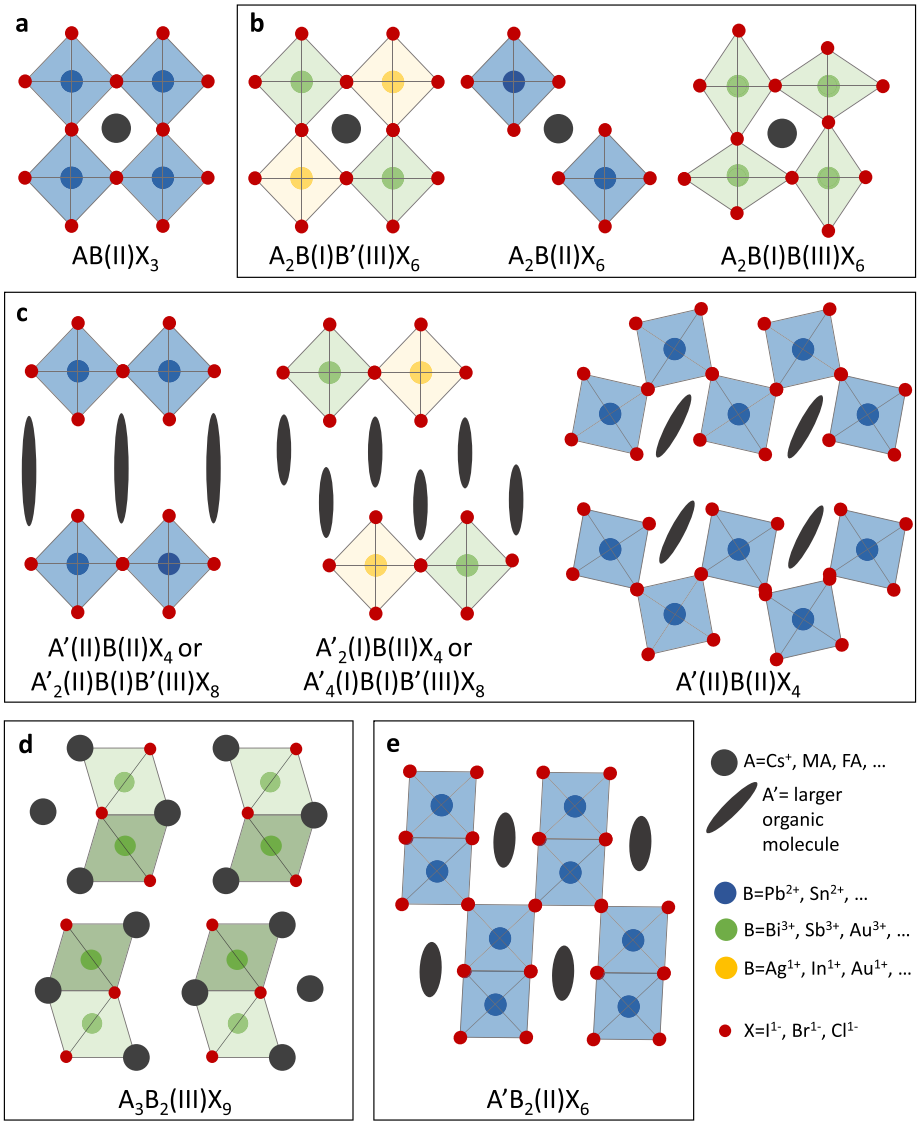

Figure 1. Overview of perovskite and perovskite-like crystal structures mentioned in this article: (a) Single perovskites, (b) double perovskites with alternating metal octahedra (left), an ordered vacancy (middle) or mixed-valence B sites (right), (c) corner-sharing quasi-2D perovskites with Dion–Jacobson (left) or Ruddlesden–Popper (middle) layer stacking. Can be derived from either a single perovskite or a double perovskite parent lattice. Corrugated structures (right) are also possible. (d) Quasi-0D material with face-sharing metal-halide octahedra, (e) extended perovskite-analogue with edge-sharing octahedral dimers with 3D corner-sharing connectivity.

temperature [24] belongs to the *Pnma* symmetry group and corresponds to a $a^+b^-b^-$ tilt pattern (labeled in Glazer notation [25])[3].

2.2. Double perovskites

As their name suggests, double perovskites double the single perovskite formula, leading to a broad class of materials with formula $A_2BB'X_6$[4]. In our classification of these materials, we use the definition by Wolf *et al* which consists of the following criteria reproduced here for convenience [27]:

(i) The structure contains cations or vacancies surrounded by six halides $[BX_6]^{n-}$, where B can be a cation or a vacancy.
(ii) The $[BX_6]^{n-}$ units are exclusively corner-sharing in a 3D pattern.

[3] In Glazer notation the tilt pattern is divided into rotations around the cartesian *a*, *b*, and *c* axes, denoted by sets of three letters. Superscripts +, −, and 0 refer to in-phase, out-of-phase and no rotation, respectively.
[4] Metal-halide double perovskites are also called elpasolites, named after the mineral K_2NaAlF_6, that was discovered in the Rocky Mountains and first described in 1883 [26].

(iii) There are exactly two structurally distinguishable $[BX_6]^{n-}$ motifs in the unit cell, such that the chemical formula must be $A_2BB'X_6$.

This classification also includes vacancy-ordered perovskites A_2BX_6, which do not feature corner-sharing octahedra but share important similarities related to their electronic structure with double perovskites consisting of two different metal-centered B sites (see section 5.2). The definition also includes materials with mixed-valence B sites, such as $Cs_2Au(I)Au(III)I_6$ (figure 1(b)).

Halide double perovskites can feature B sites with nominal oxidation states varying between +1 and +4, allowing in principle for tens of thousands of stable elemental combinations [28, 29]. All known halide double perovskites crystallize in a rocksalt structure with alternating $[BX_6]^{n-}$ and $[B'X_6]^{n-}$ octahedra favored by electrostatics. For a more complete review of the structures and chemical composition of halide double perovskites, we refer the reader to [27, 30, 31].

2.3. Quasi-2D perovskites

Quasi-2D perovskites are common derivatives of the 3D perovskites which maintain the corner-sharing octahedral building blocks, but only in two, rather than three dimensions, yielding alternating layers of octahedral networks and non-bonding cations [32, 33]. In organic-inorganic halide perovskites, incorporation of large organic cations gives rise to a great degree of control over the shape, alignment and thickness of the metal-halide layers (see for example figure 1(c)), and consequently to a significant broadening of this materials family [34]. For example, depending on the structure and valence of the organic cation, the metal-halide layers may be misaligned, fully aligned (or anywhere in between) [35], or the layers may be corrugated instead of flat [36].

In this review, we will mainly discuss the Ruddlesden–Popper series with chemical formula, $A_{n-1}A'_2B_nX_{3n+1}$, where A is an inorganic or organic monovalent cation, and A' usually is a large bulky organic molecule, such as butylammonium or phenethylammonium, but can also be an inorganic cation such as Cs^+ [37]. In the chemical formula above, n refers to the number of perovskite layers per unit cell, where $n = \infty$ would correspond to a 3D ABX_3 single perovskite. Furthermore, similar to the 3D single perovskites, quasi-2D perovskite structures can be extended to allow for double perovskite stoichiometries with alternating B and BB′ sites [38] (see section 2.2).

2.4. Other quasi-low-dimensional and Perovskite-like materials

A number of structural motifs exist that do not fall into any of the above categories, but are often classified as perovskites or perovskite-like in the literature, either because they feature $[BX_6]^{n-}$ octahedra or because their electronic structure is reminiscent of that of traditional halide perovskites. One example is given by structures with corner-sharing connectivity in one dimension, which have recently been reported [39, 40]. Another example are materials with formula $A_3B_2X_9$, where B is a trivalent cation such as Bi^{3+} which is isoelectronic to Pb^{2+} with a $6s^2$ lone pair. In $A_3Bi_2X_9$ with A = Cs^+ or MA, two $[BiX_6]^{3-}$ octahedra arrange in pairs of face-sharing connectivity, but do not form bonds with neighboring units (figure 1(d)) [41–44]. Similarly, edge-sharing octahedra can serve as the basic building blocks, e.g. in the so-called expanded perovskite analogues. These feature corner-connected $[B_2X_{10}]^{6-}$ dimers (B = Sn^{2+}, Pb^{2+}) and allow for the incorporation of significantly larger aromatic A site molecules like dimethylpyrazinium and aminomethylpyridinium (figure 1(e)) [45–49].

3. Overview of first-principles methods

In this article, we concentrate on two frameworks for calculating ground and excited-state properties of materials: DFT and Green's function-based MBPT using the *GW* Bethe–Salpeter equation (BSE) approaches. In the following, we will sketch the basics of these methods with a focus on the calculation of optoelectronic properties of solids such as bandstructures, optical absorption spectra and electron–phonon coupling. We adapt a spin-unpolarized notation for clarity of the presentation, while fully acknowledging that spin–orbit coupling strongly affects the optoelectronic properties of many halide perovskites. A fully relativistic treatment of spin–orbit interactions is available in most DFT and *GW*+BSE computational packages including some of the codes most popularly used in the study of perovskites, such as QUANTUM ESPRESSO [50], VASP [51–53], BERKELEYGW [54, 55], and YAMBO [56]. In the following, we will use Hartree atomic units throughout.

3.1. DFT

3.1.1. Foundations of DFT

DFT is based on the Hohenberg–Kohn theorem which states that all quantum-mechanical ground-state observables can in principle be obtained as functionals of the ground-state density $n(\mathbf{r})$. The Hamiltonian of a system of N interacting electrons is $H = T + V_{\text{ext}} + W$ in the Born–Oppenheimer approximation, where T is the kinetic energy operator, $V_{\text{ext}} = \sum_{i=1}^{N} v_{\text{ext}}(\mathbf{r}_i)$ the interaction between each electron and the total external potential of the nuclei, $v_{\text{ext}}(\mathbf{r}_i)$, and W is the total electron–electron interaction [57, 58].

The Hohenberg–Kohn theorem [59] states that there is a one-to-one mapping between the external potential v_{ext}, the ground-state wavefunction $|\Psi_0\rangle$ and the ground-state density $n(\mathbf{r})$. Thus, $|\Psi_0\rangle$, which is obtained by solving $H|\Psi_0\rangle = E_0|\Psi_0\rangle$, is a unique functional of the density, and so are all ground-state observables including the ground-state energy. Furthermore, the Hohenberg-Kohn theorem implies that the exact ground-state density and energy, can in principle be obtained by minimizing the total-energy functional

$$E[n] = F[n] + \int \mathrm{d}^3 r v_{\text{ext}}(\mathbf{r})\, n(\mathbf{r}) \tag{1}$$

where $F[n] = \langle \Psi[n] | T + W | \Psi[n] \rangle$ is a universal functional, independent of $v_{\text{ext}}(\mathbf{r})$ and the notation $\Psi[n]$ denotes that the wavefunction Ψ is a unique functional of the ground-state density.

The Kohn–Sham equations [60] can be derived by first reformulating the energy functional of a system of N interacting electrons as below, and minimizing this functional with respect to n:

$$E[n] = T_s[n] + E_{\text{H}}[n] + E_{\text{ext}}[n] + E_{\text{xc}}[n], \tag{2}$$

where T_s is the kinetic energy of a system of N *non-interacting* electrons (to be distinguished from T, the kinetic energy of the *interacting* electrons), $E_{\text{H}}[n]$ is the classical electrostatic Hartree energy, and $E_{\text{ext}}[n]$ is the energy associated with the interaction between the electrons and nuclei. $E_{\text{xc}}[n]$, the exchange-correlation functional, is thus defined as those energy terms not included in E_{H} and T_s, $E_{\text{xc}} = T - T_s + W - E_{\text{H}}$.

A key result of this derivation is the formulation of an effective local potential,

$$v^{\text{KS}}(\mathbf{r}) = v_{\text{H}}(\mathbf{r}) + v_{\text{ext}}(\mathbf{r}) + v_{\text{xc}}(\mathbf{r}), \tag{3}$$

in which v_{H} is the Hartree potential and $v_{\text{xc}} = \delta E_{\text{xc}}[n]/\delta n$ is the exchange-correlation potential. The ground-state density $n(\mathbf{r})$ of the interacting N electron system is obtained by solving the one-particle equations [61]

$$\left[-\frac{1}{2}\nabla^2 + v^{\text{KS}}(\mathbf{r})\right] \varphi_{n\mathbf{k}}(\mathbf{r}) = \varepsilon_{n\mathbf{k}} \varphi_{n\mathbf{k}}(\mathbf{r}), \tag{4}$$

where the KS states are labeled with band index n and wave vector $\mathbf{k}$, and summing over all occupied orbitals $\varphi_{n\mathbf{k}}(\mathbf{r})$

$$n(\mathbf{r}) = \sum_{n,\mathbf{k}} |\varphi_{n\mathbf{k}}(\mathbf{r})|^2. \tag{5}$$

In practical calculations, $v_{\text{H}}(\mathbf{r})$ and $v_{\text{ext}}(\mathbf{r})$ have well defined analytical expressions, while v_{xc} needs to be approximated, as discussed in section 3.1.3.

3.1.2. Generalized KS equations

The generalized KS approach is an important and practically useful extension of KS-DFT that allows for the mapping of the real interacting many-electron problem to all possible solutions that can be expressed as a single Slater determinant [62–64]. In this approach, $F[n]$ (equation (1)) is partitioned as $F[n] = F_S[n] + R_S[n]$, where F_S is obtained by minimization of a Slater-determinant-dependent functional $S[\Phi] = S[\{\varphi_{n\mathbf{k}}\}]$, where the Slater determinant Φ is constructed from the set of orbitals $\{\varphi_{n\mathbf{k}}\}$. $R_S[n]$ is the 'remainder' density functional that depends on the choice of S. The total energy is then

$$E[n\{\varphi_{n\mathbf{k}}\}] = S[\{\varphi_{n\mathbf{k}}\}] + R_S[n[\{\varphi_{n\mathbf{k}}\}] + E_{\text{ext}}[n\{\varphi_{n\mathbf{k}}\}], \tag{6}$$

and the corresponding generalized KS equations

$$\left(\hat{O}_S[\{\varphi_{n\mathbf{k}}\}] + v_{R_S} + v_{\text{ext}}\right) \varphi_{n'\mathbf{k}'} = \varepsilon_{n'\mathbf{k}'} \varphi_{n'\mathbf{k}'}, \tag{7}$$

in which $\hat{O}_S[\{\varphi_{n\mathbf{k}}\}]$ is a non-local operator defined as

$$\frac{\delta S[\{\varphi_{n\mathbf{k}}\}]}{\delta \varphi^*_{n'\mathbf{k}'}} = \hat{O}_S[\{\varphi_{n\mathbf{k}}\}]\,\varphi_{n'\mathbf{k}'}, \tag{8}$$

and $v_{R_S}(\mathbf{r}) = \delta R_S[n]/\delta n(\mathbf{r})$. The ground-state density is obtained from equation (5) by summing over all occupied orbital densities calculated self-consistently.

Note that if S is chosen as the kinetic energy of the Slater determinant Φ, $S[\Phi] = \langle \Phi | T | \Phi \rangle$, equation (6) reduces to the regular KS total energy with $\hat{O}_S[\{\varphi_{n\mathbf{k}}\}] = -\nabla^2/2$ and $R_S[n] = E_\mathrm{H}[n] + E_\mathrm{xc}[n]$. Conversely, when $S[\Phi] = \langle \Phi | T + W | \Phi \rangle$ and $R_S[n] = 0$, the generalized KS equations take the form of the Hartree–Fock equations:

$$\left[-\frac{1}{2}\nabla^2 + v_\mathrm{H}(\mathbf{r}) + v_\mathrm{ext}(\mathbf{r})\right]\varphi_{n'\mathbf{k}'}(\mathbf{r}) - \int \mathrm{d}^3 r' \sum_{n,\mathbf{k}} \frac{\varphi^*_{n\mathbf{k}}(\mathbf{r}')\,\varphi_{n\mathbf{k}}(\mathbf{r})}{|\mathbf{r}-\mathbf{r}'|}\varphi_{n'\mathbf{k}'}(\mathbf{r}) = \varepsilon_{n'\mathbf{k}'}\varphi_{n'\mathbf{k}'}(\mathbf{r}). \tag{9}$$

3.1.3. Exchange-correlation approximations

This section will provide a brief overview of common exchange-correlation approximations and refer the reader to [58, 63, 65] for comprehensive discussions. All common exchange-correlation functionals mentioned in the following can be employed in a generalized KS framework, which reduces to the regular KS equations whenever there is no explicit orbital dependence in the exchange-correlation energy. Conceptual differences between the KS and generalized KS approaches arise in the interpretation of their single-particle eigenvalues and will be discussed in section 3.1.4.

In the local density approximation (LDA), e_xc, the exchange-correlation energy per electron is approximated locally to that of the homogeneous electron gas, which is exactly known [61]:

$$E_\mathrm{x}^\mathrm{LDA}[n] = -\frac{3}{4}\left(\frac{3}{\pi}\right)^{1/3}\int \mathrm{d}^3\mathbf{r}\, n(\mathbf{r})^{4/3}. \tag{10}$$

The correlation energy is obtained through parametrizations of Quantum Monte Carlo calculations [66], such as the ones by Vosko *et al* [67], Perdew and Zunger [68], and Perdew and Wang [69].

Generalized gradient approximations (GGAs) are analytical expressions for the exchange-correlation energy that include gradients of the electron density and usually result in energies and forces that are more accurate than those obtained with the LDA [58]:

$$E_\mathrm{xc}^\mathrm{GGA}[n] = \int \mathrm{d}^3 r f(n(\mathbf{r}), \nabla n(\mathbf{r})). \tag{11}$$

The function $f(n(\mathbf{r}), \nabla n(\mathbf{r}))$ can be constructed by satisfying exact constraints, e.g. the expression derived by Perdew, Burke and Ernzerhof (PBE) [70], by fitting to thermochemical or other empirical data [71] or a combination thereof [72, 73].

The LDA and GGAs are used routinely for the calculation of ground-state properties, high-throughput applications [74–78], and the training of machine-learning models [28, 79–85] due to their reasonable accuracy and computational cost. However, they suffer from well-known shortcomings such as a failure to predict fundamental band gaps of solids (see section 3.1.4), and an inaccurate description of charge localization and distribution between subsystems [86], and charge transfer [87, 88] in molecular systems.

These shortcomings can be alleviated to some extent by constructing hybrid functionals which combine (semi)local exchange and correlation with fractions of exact exchange (EXX) of the form [89]:

$$E_\mathrm{x}^\mathrm{EXX} = -\frac{1}{2}\sum_{i,j}^{N}\int \mathrm{d}^3 r \mathrm{d}^3 r' \frac{\varphi^*_{n\mathbf{k}}(\mathbf{r})\,\varphi^*_{n'\mathbf{k}'}(\mathbf{r}')\,\varphi_{n'\mathbf{k}'}(\mathbf{r})\,\varphi_{n\mathbf{k}}(\mathbf{r}')}{|\mathbf{r}-\mathbf{r}'|}. \tag{12}$$

Global hybrid functionals consist of a fixed fraction of EXX α and semilocal exchange and correlation. In the generalized KS framework, these functionals have the form [90]:

$$S[\Phi] = \langle \Phi | T + \alpha W | \Phi \rangle \tag{13}$$

$$R_S[n] = (1-\alpha)\left(E_\mathrm{H}[n] + E_\mathrm{x}^\mathrm{sl}[n]\right) + E_\mathrm{c}^\mathrm{sl} \tag{14}$$

where E_x^sl and E_c^sl are semilocal expressions for exchange and correlation energies. The parameter α of popular hybrid functionals has been determined by fitting to extensive molecular data sets [91] or by using the adiabatic connection formula [92]. For example, $\alpha = 0.25$ for the global hybrid functional PBE0 [89, 93].

The premise of range-separated hybrid (RSH) functionals is that EXX and semilocal exchange dominate the total exchange-correlation energy at different electron-electron distances r [94, 95], and can therefore be constructed by separating the Coulomb interaction W into a long-range and a short-range term via

$$\frac{1}{r} = \frac{\alpha + \beta \mathrm{erf}(\gamma r)}{r} + \frac{1 - [\alpha + \beta \mathrm{erf}(\gamma r)]}{r}, \tag{15}$$

where α is the fraction of short-range EXX, $\alpha + \beta$ the fraction of long-range EXX, and γ is the range-separation parameter [96–101]. Assuming range-independent semilocal correlation, this amounts to the following expression in a generalized KS framework:

$$S[\Phi] = \langle \Phi | T | \Phi \rangle + \alpha E_{\mathrm{x,SR}}^{\mathrm{EXX}} + (\alpha + \beta) E_{\mathrm{x,LR}}^{\mathrm{EXX}} \tag{16}$$

$$R_S[n] = E_{\mathrm{H}}[n] + (1 - \alpha) E_{\mathrm{x,SR}}^{\mathrm{sl},\gamma}[n] + (1 - \alpha - \beta) E_{\mathrm{x,LR}}^{\mathrm{sl},\gamma} + E_{\mathrm{c}}^{\mathrm{sl}}[n]. \tag{17}$$

In atoms, molecules and clusters, the correct asymptotic behavior of the exchange-correlation potential is ensured by requiring $\alpha + \beta = 1$, while in solids, an on-average correct description of long-range dielectric screening effects is taken into account by ensuring that $\alpha + \beta = 1/\epsilon_\infty$, where ϵ_∞ is the orientationally-averaged high-frequency dielectric constant. The parameter α mixes semilocal exchange and correlation and EXX at short range, and is often set to $\alpha = 0.25$, similar to its use in global hybrid functionals. The parameter γ can be tuned to satisfy exact criteria, such as the ionization potential theorem of DFT (see section 3.1.4). This 'optimally tuned (screened) RSH' (OT-SRSH) approach has been applied with great success to finite systems [64, 95, 102] and molecular crystals [103]. In addition, references [104, 105] tuned the parameter γ such that band gaps match quasiparticle *GW* calculations, demonstrating that these functionals can yield *GW* quality band structures. Most recently, reference [106] used localized Wannier functions to enforce the ionization potential theorem and formulate an inexpensive and non-empirical method of optimally tuning the SRSH parameters. The Wannier OT-RSH functional (WOT-SRSH) developed in reference [106] has since been successfully used to calculate quasiparticle band gaps for standard III-V and II-VI semiconductors and insulators [106], oxides [107] and halide perovskites [108], as well as a starting point for MBPT calculations with improved accuracy [107, 109].

Finally, meta-GGAs such as the SCAN [110] and TASK [111] functionals, include a dependence on the KS kinetic energy density and/or the Laplacean of the charge density, and have been constructed to satisfy other analytical properties such as the derivative discontinuity of the exact exchange-correlation functional than typical (semi)local approximations. Meta-GGAs have been shown to yield more accurate predictions of total energies (SCAN) [110] and improved band gaps at a computational cost comparable to that of semilocal xc approximations (TASK) [112].

3.1.4. Interpretation of (generalized) KS eigenvalues

Solving the KS equations (equations (3)–(5)) or the generalized KS equations (equation (7)) results in an eigenvalue spectrum, or in the case of solids a band structure. KS eigenvalues have a well-defined meaning as zeroth-order approximations to excitation energies [113], but are not equal to electron addition and removal energies, with the exception of the energy of the highest occupied state, which is equivalent to the negative ionization potential [114–116].

The fundamental band gap, E_{gap}, is defined as the energy difference between the ionization energy $I(N)$ and the electron affinity $A(N)$, and can in principle be calculated from the total energies of an N-electron system, and the same system in which an electron has been removed $(N-1)$ and added $(N+1)$, respectively [63]:

$$E_{\mathrm{gap}}(N) = I(N) - A(N) = [E(N-1) - E(N)] - [E(N) - E(N+1)]. \tag{18}$$

In practical calculations, the energy difference between the valence band maximum (VBM), $\varepsilon_{\mathrm{VBM}}$, and the conduction band minimum (CBM) $\varepsilon_{\mathrm{CBM}}$, is often associated with E_{gap}. However, when $\varepsilon_{\mathrm{CBM}}$ and $\varepsilon_{\mathrm{VBM}}$ are calculated within KS DFT, $E_{\mathrm{gap}}^{\mathrm{KS}} = \varepsilon_{\mathrm{CBM}} - \varepsilon_{\mathrm{VBM}}$ is not equal to E_{gap}, due to the so-called derivative discontinuity, the constant by which the KS potential has to jump upon addition or removal of an electron [117–119]. (Semi)local approximations of the exchange-correlation functional do not include a derivative discontinuity [63].

Fundamental band gaps calculated with hybrid functionals and meta-GGAs are often in better agreement with experiment because they are typically implemented in a generalized KS framework [120]. Equation (7) shows that the exchange-correlation potential of generalized KS theory includes an integral operator. This allows in principle for the equality $E_{\mathrm{gap}} = E_{\mathrm{gap}}^{\mathrm{gKS}}$ to hold because the derivative discontinuity is (partially)

incorporated in the generalized KS band gap [120]. In practice, the accuracy of band gaps calculated with hybrid functionals and meta-GGAs is material-dependent and can also rely on the specific tuning procedure used to determine its parameters, for example as described in [104–106].

3.2. MBPT

3.2.1. The GW approximation

The GW approximation is a state-of-the-art methodological framework used to understand electron addition and removal, i.e. charged electronic excitations, in functional materials. *GW* band gaps and band structures in general yield good agreement with results from photoemission experiments for a broad variety of materials, ranging from molecules and clusters to bulk and nanostructured solids [121–127]. In this section, we will sketch some of the basic equations which are directly relevant to practical calculations of quasiparticle band structures in halide perovskites without attempting any derivations, and refer the reader to comprehensive reviews of the *GW* method, such as [128–130] and references therein.

The premise of the *GW* approximation is that addition and removal of an electron is described by a so-called 'quasiparticle' (QP). Intuitively, a QP is pictured as an electron (or hole) surrounded by a 'cloud' of opposite charges corresponding to the response of the polarizable charge density to the addition or removal of an electron [128]. QPs have corresponding Dyson orbitals $\varphi^{\mathrm{QP}}_{n\mathbf{k}}$ and energies $\varepsilon^{\mathrm{QP}}_{n\mathbf{k}}$, which are calculated by solving the Dyson equation,

$$\left[-\frac{1}{2}\nabla^2 + v_{\mathrm{H}}(\mathbf{r}) + v_{\mathrm{ext}}(\mathbf{r})\right]\varphi^{\mathrm{QP}}_{n\mathbf{k}}(\mathbf{r}) + \int \mathrm{d}^3 r' \Sigma\left(\mathbf{r},\mathbf{r}',\varepsilon^{\mathrm{QP}}_{n\mathbf{k}}\right)\varphi^{\mathrm{QP}}_{n\mathbf{k}}(\mathbf{r}') = \varepsilon^{\mathrm{QP}}_{n\mathbf{k}}\varphi^{\mathrm{QP}}_{n\mathbf{k}}(\mathbf{r}), \tag{19}$$

where the QP state is labeled with band index n and wave vector $\mathbf{k}$. $\Sigma(\mathbf{r},\mathbf{r}';\varepsilon^{\mathrm{QP}}_{n\mathbf{k}})$ is the electron self-energy, which in the *GW* approximation, is computed as the frequency space convolution of the non-interacting Green's function, G, and the screened Coulomb potential, W. The electron self-energy is in general a complex, energy dependent operator, and contains information about both the energy shift due to inclusion of electron-electron interactions (real part) and the lifetime of the QPs (imaginary part) [130].

In practice, *GW* QP energies are often calculated as perturbative corrections to a single-particle Hamiltonian, e.g. that of Hartree–Fock or (generalized) KS DFT [130, 131]. For an example, consider the generalized KS equations (equation (7)) with a non-local exchange-correlation potential $v_{\mathrm{xc}}(\mathbf{r},\mathbf{r}')$,

$$\left[-\frac{1}{2}\nabla^2 + v_{\mathrm{H}}(\mathbf{r}) + v_{\mathrm{ext}}(\mathbf{r})\right]\varphi^{g\mathrm{KS}}_{n\mathbf{k}}(\mathbf{r}) + \int \mathrm{d}^3 r' v_{\mathrm{xc}}(\mathbf{r},\mathbf{r}')\varphi^{g\mathrm{KS}}_{n\mathbf{k}}(\mathbf{r}') = \varepsilon^{g\mathrm{KS}}_{n\mathbf{k}}\varphi^{g\mathrm{KS}}_{n\mathbf{k}}(\mathbf{r}), \tag{20}$$

with eigenvalues $\varepsilon^{g\mathrm{KS}}_{n\mathbf{k}}$ and corresponding eigenfunctions $\varphi^{g\mathrm{KS}}_{n\mathbf{k}}$. Assuming that $\varphi^{g\mathrm{KS}}_{n\mathbf{k}} \approx \varphi^{\mathrm{QP}}_{n\mathbf{k}}$, QP eigenvalues can be calculated in lowest order perturbation theory (typically referred to as G_0W_0) with equations (19) and (20):

$$\varepsilon^{\mathrm{QP}}_{n\mathbf{k}} = \varepsilon^{g\mathrm{KS}}_{n\mathbf{k}} + \langle\varphi^{g\mathrm{KS}}_{n\mathbf{k}}|\Sigma\left(\varepsilon^{\mathrm{QP}}_{n\mathbf{k}}\right) - v_{\mathrm{xc}}|\varphi^{g\mathrm{KS}}_{n\mathbf{k}}\rangle. \tag{21}$$

In G_0W_0, the self-energy is calculated as [130]:

$$\Sigma(\mathbf{r},\mathbf{r}',\omega) = \mathrm{i}\int \mathrm{d}\omega' \mathrm{e}^{\mathrm{i}\delta^+\omega'} G_0(\mathbf{r},\mathbf{r}',\omega-\omega') W_0(\mathbf{r},\mathbf{r}',\omega'), \tag{22}$$

where δ^+ is a small positive constant, $G_0(\mathbf{r},\mathbf{r}',\omega) = \sum_{n\mathbf{k}} \frac{\varphi^{g\mathrm{KS}}_{n\mathbf{k}}(\mathbf{r})\varphi^{*g\mathrm{KS}}_{n\mathbf{k}}(\mathbf{r}')}{\omega-\varepsilon_{n\mathbf{k}}+\mathrm{i}\eta}$ (with η a positive or negative constant for occupied and unoccupied states, respectively) and $W_0(\mathbf{r},\mathbf{r}',\omega) = \int \mathrm{d}^3\mathbf{r}''\epsilon^{-1}(\mathbf{r},\mathbf{r}'',\omega)v(\mathbf{r}'',\mathbf{r}')$, where ϵ is the dielectric function and v is the bare Coulomb potential. The dielectric function is calculated within the random phase approximation (RPA) as:

$$\epsilon(\mathbf{r},\mathbf{r}',\omega) = \delta(\mathbf{r},\mathbf{r}') - \int \mathrm{d}^3\mathbf{r}'' v(\mathbf{r},\mathbf{r}'')\chi_0(\mathbf{r}'',\mathbf{r}',\omega) \tag{23}$$

where the irreducible polarizability χ_0 is constructed from (generalized) KS eigenfunctions and eigenvalues [132, 133].

Several approaches to G_0W_0 calculations can be distinguished at this point, depending on the approach used to calculate or approximate (i.e. using plasmon pole models [130, 134]) the frequency-dependent dielectric function, or by neglecting the frequency dependence [130]. Full-frequency calculations, while substantially more computationally demanding, allow accurate computation of the spectral function and visualization of spectral features including QP lifetimes and satellites [135, 136]. On the other hand, plasmon-pole model approximations for the dielectric function are popular for calculations of QP band gaps

and band structures. The choice of plasmon-pole model can lead to differences in computed band gaps of up to 1 eV, which are highly system dependent [137]. Larson *et al* [137] highlights that the plasmon-pole model by Godby and Needs [134] yields good agreement with full-frequency calculations in a range of standard semiconductors and insulators.

G_0W_0 QP band gaps are generally sensitive to the single-particle starting point used to construct G_0 and W_0. For example, with a semi-local PBE starting point, QP band gaps for a wide variety of semiconductors and insulators are underestimated with respect to experiment by an average of 0.4 eV, while starting from generalized KS eigenvalues and eigenfunctions calculated with hybrid functionals such as PBE0, HSE and WOT-SRSH yields improved mean absolute errors with respect to experiment of 0.31 eV, 0.22 eV and 0.19 eV, respectively [109]. Similar trends were also shown in the G_0W_0 band gaps of halide perovskites [138–141] (see section 4.1.2). Implementation of self-consistency in the *GW* approximation is another route to mitigating the starting-point dependence for QP band gaps. Eigenvalue self-consistent *GW* (ev*GW*) uses the eigenvalues obtained by solving equation (21) to re-calculate *G* and/or *W* until convergence is reached [142]. QP self-consistent *GW* (QS*GW*) additionally includes an update in the QPs states, by updating the generalized KS potential iteratively [143, 144]. Both ev*GW* and QS*GW* generally yield QP band gaps overestimated with respect to experiment with mean absolute errors of 0.66 eV and 0.51 eV respectively, as discussed in [109]. This significant overestimation is in part due to the absence of vertex corrections [145]. In the context of halide perovskites, reference [146] used a vertex-corrected quasiparticle-selfconsistent *GW* scheme to calculate band gaps of inorganic halide perovskites which were found to be in very good agreement with experiment after accounting for thermal effects and spin–orbit coupling. However, the magnitude of vertex corrections was not reported in this work.

Finally, we note that while calculated *GW* QP band gaps can be sensitive to different approximation and parameter choices, distinct implementations of the *GW* approximation within the BERKELEYGW [54], YAMBO [56] and ABINIT [147] computational packages yield band gaps in remarkably good agreement (within 0.1 eV) when equivalent parameters are used [127].

3.2.2. BSE

The BSE is the state-of-the-art framework for computing neutral excitations in semiconductors and insulators [148–150], describing the interaction between correlated electrons and holes upon photoexcitation. In the following, we will focus only on the Tamm–Dancoff approximation (which neglects de-excitation) to the BSE, most commonly used in inorganic semiconductors and insulators. A general discussion and derivation of this theoretical framework can be found, for example, in the seminal references by Strinati [148] and Rohlfing and Louie [149, 150]. In the Tamm–Dancoff approximation, the BSE is written as [150]:

$$\left(\varepsilon^{\mathrm{QP}}_{c\mathbf{k}_\mathrm{e}} - \varepsilon^{\mathrm{QP}}_{v\mathbf{k}_\mathrm{h}}\right) A^S_{c\mathbf{k}_\mathrm{e}v\mathbf{k}_\mathrm{h}} + \sum_{c'\mathbf{k'}_\mathrm{e}v'\mathbf{k'}_\mathrm{h}} \langle c\mathbf{k}_\mathrm{e}v\mathbf{k}_\mathrm{h}|K^{\mathrm{eh}}|c'\mathbf{k'}_\mathrm{e}v'\mathbf{k'}_\mathrm{h}\rangle A^S_{c'\mathbf{k'}_\mathrm{e}v'\mathbf{k'}_\mathrm{h}} = \Omega^S\left(\mathbf{k}_\mathrm{e} - \mathbf{k}_\mathrm{h}\right) A^S_{c\mathbf{k}_\mathrm{e}v\mathbf{k}_\mathrm{h}}, \tag{24}$$

where $\varepsilon_{c(v)\mathbf{k}_{\mathrm{e(h)}}}$ are the QP energies of occupied (v) and unoccupied (c) single-particle states, $|c\mathbf{k}_\mathrm{e}v\mathbf{k}_\mathrm{h}\rangle$ is the direct product of occupied and unoccupied single-particle states, $A^S_{c\mathbf{k}_\mathrm{e}v\mathbf{k}_\mathrm{h}}$ are the coefficients of the exciton wavefunction in the single-particle basis corresponding to the state S with energy Ω_S and K^{eh} is the electron–hole kernel. We highlight here that in the expressions above we have assumed for the sake of completeness that excitons carry a finite momentum equal to $\mathbf{Q} = \mathbf{k}_\mathrm{e} - \mathbf{k}_\mathrm{h}$. In most practical calculations of linear optical absorption spectra or exciton binding energies, it is sufficient to compute zero-momentum excitons [151], and for this reason we will limit our discussion only to the case of $\mathbf{k}_\mathrm{e} = \mathbf{k}_\mathrm{h}$. It is however important to note that finite momentum excitons play a key role in the physics of exciton-phonon interactions which underpins important phenomena such as exciton dynamics, exciton diffusion and radiative recombination [152–157].

K^{eh} is typically expressed as a sum of a frequency-independent exchange and a frequency-dependent direct component [150]. The exchange term is repulsive and its contribution corresponds to the energy difference between singlet and triplet excitonic states in systems with negligible spin–orbit coupling [152, 158]. The direct term is attractive and carries with it the characteristics of the dielectric function, such as its non-locality and frequency dependence [151]. Standard implementations of the BSE generally neglect the frequency dependence of the direct kernel. This is a valid approximation for most standard semiconductors and is justified by the large difference in energy between the poles of the dielectric function and the exciton binding energy [149]. The frequency dependence of the dielectric function has been shown to be important for systems with very large exciton binding energies, such as carbon nanotubes [159, 160], or when the contribution of polar ionic vibrations to the dielectric function are significant (e.g. in some halide perovskites) [161–164].

The eigenvalues Ω_S and eigenvectors $A^S_{cv\mathbf{k}}$ of equation (24) are the corresponding excitation energies, directly connected to the exciton binding energy, $E_\mathrm{B} = E^\mathrm{QP}_\mathrm{gap} - \Omega_1$, and the exciton wave function $\Psi^S(\mathbf{r_e}, \mathbf{r_h}) = \sum_{cv\mathbf{k}} A^S_{cv\mathbf{k}} \varphi^*_{v\mathbf{k}}(\mathbf{r}_\mathrm{h}) \varphi_{c\mathbf{k}}(\mathbf{r}_\mathrm{e})$. The latter can be used to calculate the spatial distribution of photogenerated electron–hole pairs and for example identify charge transfer or interlayer excitons [165–168]. In addition, from the solution of equation (24), the imaginary part of the macroscopic transverse dielectric function can be calculated as

$$\epsilon_2(\omega) = \frac{16\pi}{\omega^2} \sum_S |\mathbf{e} \cdot \langle 0|\mathbf{v}|S\rangle|^2 \delta(\omega - \Omega_S), \tag{25}$$

where $|0\rangle$ and $|S\rangle$ correspond to the ground and excited state S, respectively, $\mathbf{e}$ is the light polarization vector and $\mathbf{v}$ is the velocity operator. The imaginary dielectric function thus calculated can be directly compared with experimental optical absorption spectra.

3.3. Electron–phonon interactions

The theoretical framework described up to now is not sufficient to understand phenomena in which the vibrations of ions plays a fundamental role, because it relies on the premise that ions in materials are clamped. The interaction between electrons and ionic vibrations (electron–phonon interactions) must instead be computed explicitly. Electron–phonon interactions are fundamental to key optoelectronic properties of semiconductors and insulators, including the temperature-dependence of the electronic band structure and band gap, charge-carrier mobilities, and recombination, as well as optical absorption and photoluminescence (PL) [169]. In this section, we will present a brief overview of some of the key theoretical concepts necessary to compute electron–phonon interactions in functional semiconductors (and specifically halide perovskites). As with the *GW* approximation, our brief summary will not include any derivations, and instead we refer the interested reader to reference [169] for a comprehensive review of the theory of electron–phonon interactions in the context of modern first-principles methods.

The impact of electron–phonon interactions on electronic properties of semiconductors can be computed in an analogous way to the *GW* approximation, via the electron–phonon self energy Σ^eph. Consequently, electron–phonon interactions lead to renormalized energy eigenvalues, $E_{n\mathbf{k}}$, related to the real part of Σ^eph, and a finite broadening of QP eigenstates, $\Gamma_{n\mathbf{k}}$, described by the imaginary part of Σ^eph [169]:

$$\begin{aligned} E_{n\mathbf{k}} &= \varepsilon_{n\mathbf{k}} + \mathrm{Re}\, \Sigma^\mathrm{eph}_{nn\mathbf{k}}(E_{n\mathbf{k}} + \mathrm{i}\Gamma_{n\mathbf{k}}), \\ \Gamma_{n\mathbf{k}} &= \mathrm{Im}\, \Sigma^\mathrm{eph}_{n\mathbf{k}}(E_{n\mathbf{k}} + \mathrm{i}\Gamma_{n\mathbf{k}}), \end{aligned} \tag{26}$$

where $\varepsilon_{n\mathbf{k}}$ are energy eigenvalues computed with fixed nuclei.

In most practical implementations of electron–phonon interactions, the electron–phonon self-energy consists of two main terms, namely the Fan–Migdal (FM) and the Debye–Waller (DW) terms [169]. The FM self-energy is a dynamic and complex term that describes the effect of lattice polarization on the electronic states of the clamped ionic system. The FM self-energy can be formulated in analogy with the *GW* theory as GW_ph, where W_ph is the lattice contribution to the screened Coulomb interaction [169]. In lowest-order perturbation theory, the FM self-energy can be calculated as [169]

$$\Sigma^\mathrm{FM}_{nn\mathbf{k}} = \sum_{m\nu} \int \frac{\mathrm{d}\mathbf{q}}{\Omega_\mathrm{BZ}} g^*_{mn\nu}(\mathbf{k},\mathbf{q}) g^*_{mn\nu}(\mathbf{k},\mathbf{q}) \left[\frac{1 - f_{m\mathbf{k}+\mathbf{q}} + n_{\mathbf{q}\nu}}{\omega - \varepsilon_{m\mathbf{k}+\mathbf{q}} - \omega_{\mathbf{q}\nu} + \mathrm{i}\eta} + \frac{f_{m\mathbf{k}+\mathbf{q}} + n_{\mathbf{q}\nu}}{\omega - \varepsilon_{m\mathbf{k}+\mathbf{q}} + \omega_{\mathbf{q}\nu} + \mathrm{i}\eta} \right] \tag{27}$$

where Ω_BZ is the Brillouin zone volume, η is a small positive constant, and $f_{n\mathbf{k}}$ and $n_{\mathbf{q}\nu}$ are the Fermi–Dirac and Bose Einstein occupation factors of the electronic state $|n\mathbf{k}\rangle$, with energy $\varepsilon_{n\mathbf{k}}$ and vibrational state $\mathbf{q}\nu$ with frequency $\omega_{\mathbf{q}\nu}$, respectively. $g_{mn\nu}(\mathbf{k},\mathbf{q})$ is the electron–phonon matrix element defined as $g_{mn\nu}(\mathbf{k},\mathbf{q}) = \langle m\mathbf{k}+\mathbf{q}|\Delta_{\mathbf{q}\nu} v^\mathrm{KS}|n\mathbf{k}\rangle$, with $\Delta_{\mathbf{q}\nu} v^\mathrm{KS}$ the derivative of the KS potential along the direction of a phonon mode with branch index ν, wave vector $\mathbf{q}$ and frequency $\omega_{\mathbf{q}\nu}$ [169]. The DW term is a static correction to electronic eigenstates due to ionic motion, which is proportional to the second derivative of the KS potentials with respect to ionic displacements [169].

In addition to renormalization of the electronic band structure and band gaps mentioned above, computing the electron–phonon self-energy from first principles also facilitates the understanding of charge-carrier transport. In the Boltzmann theory of transport, and within the commonly used self-energy relaxation time approximation, the electron mobility tensor can be computed as [170].

$$\mu_{\alpha\beta} = -\frac{e}{n_e \Omega} \sum_{n \in \mathrm{CB}} \int \frac{\mathrm{d}\mathbf{k}}{\Omega_{\mathrm{BZ}}} \frac{\partial f_{n\mathbf{k}}}{\partial \varepsilon_{n\mathbf{k}}} v_{n\mathbf{k},\alpha} v_{n\mathbf{k},\beta} \tau_{n\mathbf{k}}, \tag{28}$$

where e is the electron charge and n_e is the electron density, Ω and Ω_{BZ} are the crystal and first BZ volumes, respectively, $v_{n\mathbf{k},\alpha} = \dfrac{\partial \varepsilon_{n\mathbf{k}}}{\partial k_\alpha}$ is the electron band velocity along Cartesian direction α, and $\tau_{n\mathbf{k}}$ is the relaxation time. This is inversely proportional to the imaginary part of the FM self-energy, taking the following expression at finite temperature [169, 170]:

$$\begin{aligned} \frac{1}{\tau_{n\mathbf{k}}} = 2\pi \sum_{m\nu} \int \frac{\mathrm{d}\mathbf{q}}{\Omega_{\mathrm{BZ}}} |g_{mn\nu}(\mathbf{k},\mathbf{q})|^2 \left(1 - f_{m\mathbf{k}+\mathbf{q}} + n_{\mathbf{q}\nu}\right) \delta\left(\varepsilon_{n\mathbf{k}} - \omega_{\mathbf{q}\nu} - \varepsilon_{m\mathbf{k}+\mathbf{q}}\right) \\ + \left(f_{m\mathbf{k}+\mathbf{q}} + n_{\mathbf{q}\nu}\right) \delta\left(\varepsilon_{n\mathbf{k}} + \omega_{\mathbf{q}\nu} - \varepsilon_{m\mathbf{k}+\mathbf{q}}\right) |. \end{aligned} \tag{29}$$

First-principles calculations of properties emerging from electron–phonon interactions are highly challenging, not least because they involve calculations of electron–phonon matrix elements for a very dense grid of points in reciprocal space, required to converge the BZ integrals in equations (27)–(29). This has been recently addressed through the implementation of interpolation techniques using localized Wannier functions [171–175], greatly reducing the computational effort and facilitating calculations of electron–phonon properties for a wide range of complex functional materials [170, 176].

4. First-principles studies of electronic, optical and transport properties of halide perovskites

The optoelectronic, transport and vibrational properties of halide perovskites have been investigated in great detail within DFT and MBPT-based methods described in the previous section, which have both guided the interpretation of experimental data, but also driven the development of new, and more predictive computational methods and frameworks for the study of excited-state properties in semiconductors and insulators. In this section we review recent computational studies of optoelectronic properties of standard ABX_3 perovskites with B = Pb^{2+}, Sn^{2+}, while in section 5 we will give an overview of how these methods have been applied to emerging perovskite-based materials beyond the ABX_3 stoichiometry. We will primarily focus on studies of the electronic band structure, optical absorption spectra as well as charge-carrier transport and recombination.

4.1. Electronic excitations in ABX_3 Halide Perovskites

4.1.1. DFT

ABX_3 halide perovskites are direct band gap semiconductors, with dispersive, parabolic band edges [177]. Electronic states at the conduction and valence band edges are dominated by contributions of the metal-halide octahedral network. Both band edges have substantial halogen-*p* character, while the B-site *s* and *p* orbitals contribute to the valence and conduction band respectively [177, 178]. In all Pb- and Sn-based ABX_3 perovskites synthesized to date, A-site cation states can be found deep below and/or high above the valence and conduction band edges, respectively, and therefore do not contribute electronically to the optical absorption spectrum in the visible region [179].

Due to the presence of metal-*p* states at the bottom of the conduction band, the bandstructures of Pb- and Sn-based ABX_3 perovskites exhibit strong spin–orbit coupling effects [180, 181]. Even *et al* [180] was the first to point out the importance of relativistic effects for the electronic structure of lead-halide perovskites, using DFT, showing that the inclusion of spin–orbit interactions reduces the band gap of $CsPbI_3$ and $MAPbI_3$ by approximately 1 eV. At the same time, it changes the conduction band edge topology to a doubly degenerate, parabolic and isotropic band which mirrors the shape of the valence band [180] (see figure 2). In the same report, it was observed that the presence of the MA cation can break the inversion symmetry of the perovskite lattice, which in combination with strong spin orbit coupling effects leads to a Rashba–Dresselhaus [182, 183] splitting of the band edges [180]. This observation has led to many subsequent studies of Rashba–Dresselhaus spin-splitting in halide perovskites, not least because it presents the attractive possibility that charge-carrier recombination may be significantly suppressed due to this

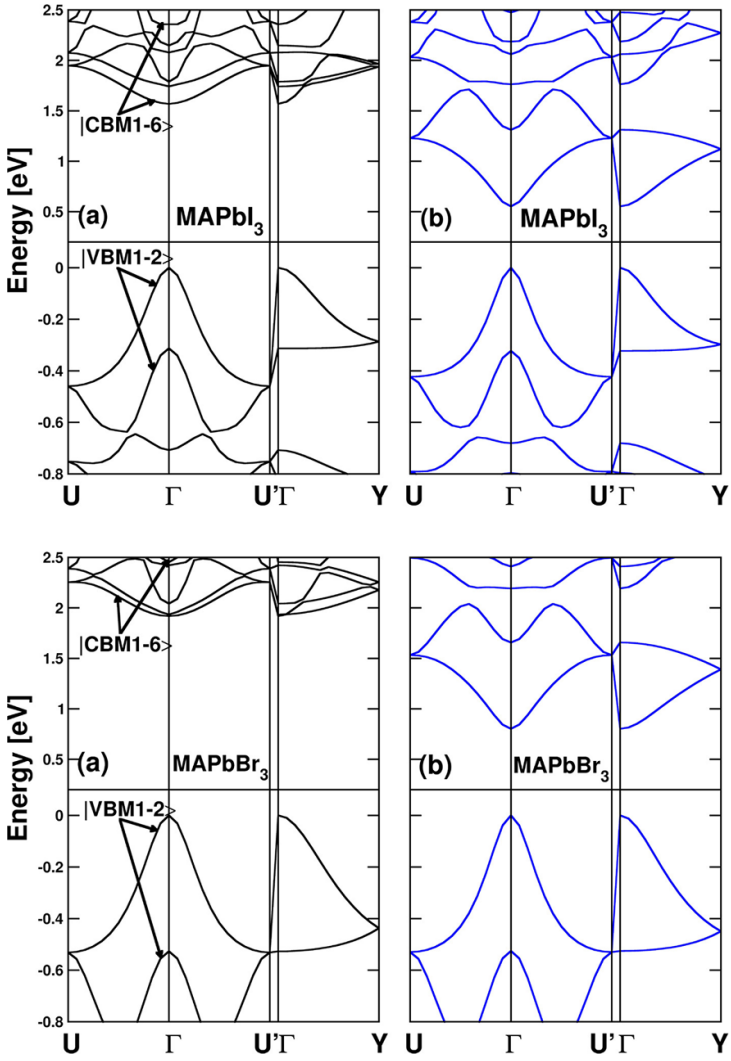

Figure 2. Electronic band structure of $MAPbI_3$ computed within DFT without (a) and with (b) spin–orbit coupling effects included in the calculation. Computational details are described in the original [180]. Reprinted with permission from [180]. Copyright 2013 American Chemical Society.

effect [184]. However, the structure of most organic-inorganic halide perovskites exhibits inversion symmetry, indicating that this effect should either occur dynamically or under the influence of external electric fields or strain [185–188]. Moreover, recent *ab initio* calculations of radiative recombination rates conclude that the slightly indirect nature of the band gap due to the occurrence of a Rashba–Dresselhaus effect decreases the recombination rate by less than a factor of two as compared to the direct band gap case [189].

Band gaps calculated within DFT methods based on the LDA or semi-local GGA exchange-correlation functionals (see section 3) are consistently underestimated with respect to experiment by more than 1 eV across the entire range of halide perovskites. Despite these discrepancies, general trends are often consistent with experiment and outline the main chemical intuition for band gap tunability in halide perovskites. Starting with the prototypical $MAPbI_3$ perovskite, the band gap increases by more than 1.5 eV by substituting I with Br or Cl, decreases by up to 0.5 eV by substituting Pb with Sn, and changes over a range of 0.2–0.3 eV by substituting the MA cation with Cs, Rb or FA [179, 190, 191]. The effects of B- and X-site substitution on the band gap can be directly linked to the composition of the band edge states [190, 191] which participate directly in optical absorption processes. On the other hand, the tunability of the band gap via the A-site cations is achieved indirectly, by volume effects and by subtly changing the structure of the inorganic lead-halide cuboctahedral network via steric interactions with the A-cations [179].

There is a broad variety of computational studies of the electronic structure properties of halide perovskites. Direct comparison between distinct studies is challenging, primarily because of the variety of atomistic models used to describe the unit cell of prototypical halide perovskites. Taking $MAPbI_3$ as an example, several independent x-ray diffraction (XRD) experiments have confirmed that its crystal structure

Table 1. Band gaps calculated for different structural phases of $MAPbI_3$ from various reports in the literature, with structures either fully optimized (opt.) or utilizing experimental lattice parameters (exp.). All calculations include relativistic effects at DFT level. The table also documents the pseudopotential (PP) type and, if available, electronic configuration of Pb and I, the xc functional used as starting point for *GW*. PP abbreviations stand for: TM-NC = Troullier–Martins norm-conserving [204], PAW = projector augmented wave [205], US = ultrasoft [206], nlcc = non-linear core corrections [207], ONCV = optimized norm-conserving Vanderbilt [208, 209]. QP band gaps calculated within the *GW* approximation either applied in a single shot (G_0W_0) or self-consistently via the QP self-consistent *GW* method [143], the 'self-consistent scissor' *GW* scheme which is wave-vector resolved ($SS_{\mathbf{k}}$-*GW* [200]) or not (SS-*GW* [139]), or by iterating self-consistently through the Green's function only. (GW_0) [142].

Structure	PP	xc functional	E_{gap}^{DFT} (eV)	*GW* type	E_{gap}^{GW} (eV)	Reference
Pnma (opt.)	TM-NC (Pb^{14+}, I^{17+})	LDA	0.58	G_0W_0	1.32	[139]
				SS-*GW*	1.79	
Pnma (opt.)	PAW (Pb^{14+}, I^{7+})	PBE	0.80	—	—	[198]
		HSE06	1.31	—	—	
		PBE0	1.92	—	—	
Pnma (exp.)	US+nlcc (Pb^{14+}, I^{17+})	LDA	0.48	G_0W_0	1.20	[75]
				SS-*GW*	1.71	
Pnma (exp.)	ONCV (Pb^{14+}, I^{25+})	PBE	0.46	G_0W_0	0.85	[199]
	ONCV (Pb^{14+}, I^{17+})	PBE	0.44	G_0W_0	1.51	
	ONCV (Pb^{14+}, I^{7+})	PBE	0.43	G_0W_0	0.87	
	ONCV (Pb^{14+}, I^{17+})	LDA	0.32	G_0W_0	1.41	
	ONCV (Pb^{14+}, I^{7+})	LDA	0.32	G_0W_0	0.98	
Pnma (exp.)	ONCV (Pb^{24+}, I^{7+})	LDA	0.47	G_0W_0	1.15	[200]
				SS-*GW*	1.57	
				$SS_{\mathbf{k}}$-*GW*	1.38	
$I4/mcm$ (opt.)	US (Pb^{14+}, I^{7+})	PBE	0.60	G_0W_0, W_0 w/o SOC	1.67	[191]
$I4/mcm$ (opt.)	US (Pb^{14+}, I^{7+})	PBE	0.53	G_0W_0, W_0 w/o SOC	1.64	[201]
$Pm\bar{3}m$	not reported	LDA	0.53	G_0W_0	1.27	[202]
				QS*GW*	1.67	
$Pm\bar{3}m$	NC	PBE	0.46	G_0W_0	1.48	[203]
$Pm\bar{3}m$ (exp.)	PAW (Pb^{24+}, I^{25+})	PBE	0.21	G_0W_0	0.94	[141]
				GW_0	1.08	
		HSE06	0.82	G_0W_0	1.26	
				GW_0	1.33	
		PBE0	1.53	G_0W_0	1.64	
				GW_0	1.65	

undergoes two phase transitions, from an orthorhombic (space group *Pnma*) to a tetragonal (space group $I4/mcm$) and finally a cubic (space group $Pm\bar{3}m$) structure, as temperature increases [24, 192, 193]. The tetragonal and cubic structures measured in XRD experiments typically report an average structure for the inorganic lead-halide network, while the organic cation is found to be fully orientationally disordered [24, 193, 194]. Therefore in practice, no long-range order can be found for these phases (and therefore periodic boundary conditions can be challenging to enforce). Instead, for $MAPbI_3$ in particular, the low temperature *Pnma* structure displays long-range order both for the inorganic network and for the orientation of the organic cations [194]. Interestingly, closely related $FAPbI_3$ does not appear to display long-range ordering even at very low temperatures [195].

First-principles computational studies of electronic structure properties rely crucially on experimental structural information, which is used either as a starting point for structural optimizations or 'out-of-the-box' structural models for electronic structure calculations. In the case of $MAPbI_3$, structural optimizations can be highly dependent on the choice of orientation for the organic cation (especially if the cubic or tetragonal case is studied), as well as on the choice of exchange correlation functional [196, 197]. Consequently, large differences in computed band gaps can be found across the literature owing to differences in these choices.

To showcase the large dispersion of band gaps reported in the literature, we compiled a (non-exhaustive) list of representative calculations of band gaps reported for $MAPbI_3$, listed in table 1. As shown in table 1, standard DFT band gaps can vary by 0.8 eV, a difference which is primarily attributed to the atomistic structure used in calculations. As will be discussed in the following, these differences are further exacerbated when calculating QP band gaps within the *GW* method, which uses DFT as a starting point.

In addition to standard local and semi-local DFT calculations, several hybrid density functionals have also been employed in order to correct for the severe underestimation of the band gap, including the global hybrid functionals PBE0 [89] and HSE [210]. Recently, RSH functionals were also employed using

parameters determined both by the dielectric response, and through a scheme enforcing Koopman's condition [211]. Bischoff *et al* [211] applied these functionals to inorganic lead-halide perovskites and found that they are a promising approach to achieve band gaps in good agreement with (but at much reduced cost than) reference MBPT calculations. This result is consistent with other studies employing RSH functionals for computing QP band gaps in standard semiconductors [104, 106]. More recently, reference [108] employed the newly developed WOT-SRSH functional to calculate band gaps of organic-inorganic halide perovskites based on Pb and Sn, and obtained agreement with experiment with a mean absolute error of approximately 0.1 eV. Furthermore, the meta-GGA TASK [111] was found to result in band gaps *on par* with those calculated using HSE, at significantly reduced computational cost [112].

4.1.2. MBPT

As discussed in section 3.2.1, the *GW* approximation is the state-of-the-art method for the accurate computation of QP band structures in semiconductors and insulators, and it has been employed in several comprehensive studies of halide perovskites. [191] was the first to report *GW* QP band gaps for $MAPbI_3$ and $MASnI_3$ (1.67 eV and 1.10 eV respectively), through an implementation of the *GW* method that included spin–orbit coupling only for the Green's function, but not for the screened Coulomb interaction, thereby achieving excellent agreement with experiment. By contrast, [202] found that accounting for SOC in the evaluation of both G and W reduces the QP correction in a single-shot G_0W_0 approximation, and leads to an underestimated QP band gap of up to 0.5 eV. This result was connected to the severely underestimated band gap of the DFT starting point, and originates in the sensitivity of G_0W_0 QP energies to "overscreening" in the mean-field [212]. Brivio *et al* [202] found that implementing self-consistency within the QP self-consistent *GW* (QSGW) method [143, 144] resolves the band gap underestimation. [139, 213] confirmed the importance of implementing self-consistency in the *GW* approximation for $MAPbI_3$ and $CsPbI_3$, using a simple eigenvalue self-consistency scheme based on subsequent rigid corrections of the band gap. This approach was later extended to a **k**-point resolved scheme, yielding largely similar corrections [200]. In addition to self-consistency, several studies have highlighted the importance of including semicore electronic states in the pseudopotential (PP) valence configuration for the metal and halogen components [146, 179, 199]. In fact, references [139, 141, 146, 199] found that QP band gaps are sensitive to the metal and halogen valence electronic configurations considered in the computational setup, highlighting the need to include a full semicore shell in order to avoid spurious error cancellations [146, 199].

As shown in table 1, there have been multiple approaches to calculate QP band gaps for lead-halide perovskites within the *GW* approximation, exploring multiple starting-points, PPs [139, 141, 199], and implementations of self-consistency [139, 202], which yield a much wider range of QP band gaps than observed at the DFT level. While we have already ascribed this observation in part to different structural configurations, different PPs, and different implementations of the *GW* approach used across these studies, the mean field starting-point dependence of QP band gaps also plays an important role. reference [141] reported a systematic study of several halide perovskites using a broad range of mean-field starting points (including semi-local DFT and hybrid functionals) and found that QP band gaps of the same perovskite can differ by up to 0.7 eV across different methodologies. The overarching conclusion of reference [141] was that a 'silver-bullet' recipe that yields QP *GW* band gaps with consistent agreement with experiment across the metal-halide perovskite family continues to remain elusive [141].

4.1.3. Temperature effects on the quasiparticle band gap

Standard DFT and *GW*+BSE implementations rely on the frozen-ion approximation. While this approximation is highly effective for understanding a wide variety of low temperature QP band gaps of semiconductors and insulators [214], temperature renormalization effects must be computed in order to compare against experiments in standard device operating conditions [215]. Temperature renormalization of the band gap in lead-halide perovskites was computed via Monte-Carlo sampling of ionic displacements, finding a renormalization of 50 meV within the harmonic phonon approximation [216]. However, molecular-dynamics-based studies have shown that anharmonic structural fluctuations lead to a more significant renormalization of the band gap [146, 217–219]. Wiktor *et al* [146] proposed a framework to compute the temperature renormalization of the band gap for the series of inorganic $CsBX_3$ perovskites using path-integral molecular dynamics and hybrid DFT calculations. According to this study, thermal fluctuations of the metal-halide perovskite lattice at room temperature increase the QP band gap calculated for the frozen-ion cubic structure by up to 0.7 eV, bringing calculated band gaps in close agreement with experimental measurements [146]. This study is also consistent with the typical differences in calculated QP band gaps found between the low temperature orthorhombic and high-temperature cubic phases [220], and indicates that octahedral tilting is present in all structural phases of halide perovskites. Interestingly, while dynamic structural distortions are not unique to halide perovskites, reference [217] found that halide and

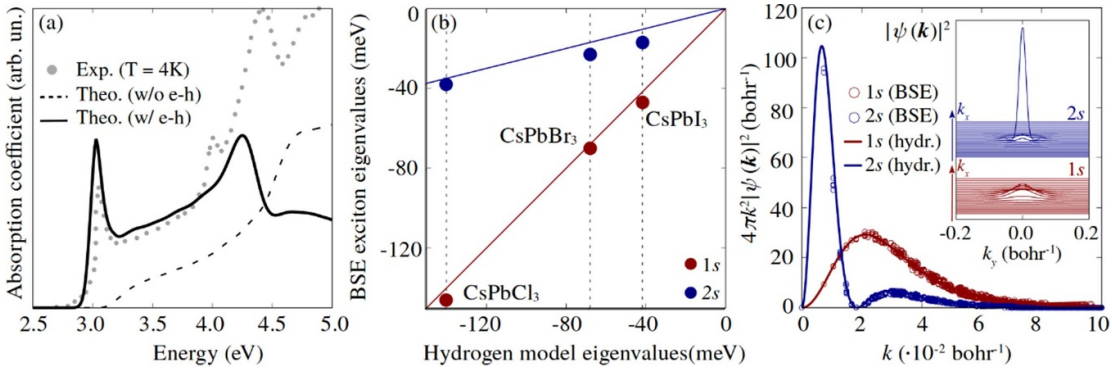

Figure 3. (a) Optical absorption spectrum of $CsPbCl_3$ computed with (continuous line) and without (dashed line) including electron–hole interactions and compared with experimental low temperature measurements (grey dots) taken from [231]. Both computed spectra are blue-shifted so as to match the onset of the experimental spectrum, as described in the original [161]. (b) and (c) Comparison between 1*s* and 2*s* exciton bound state energies (b) and radial probabilities (c) calculated from *GW*+BSE and the Wannier–Mott model. Reprinted figure with permission from [161], Copyright 2021 by the American Physical Society.

oxide perovskites exhibit opposite thermal effects on the band gaps, blue-shifting for halides and red-shifting for oxides. This is in large part due to the impact of static local symmetry-breaking distortions (polymorphism), which are found to red-shift band gaps of oxide perovskites (cancelling out the effect of dynamic distortions) but blue-shift band gaps of halide perovskites. Indeed, including polymorphism and anharmonic electron–phonon coupling using the special-displacement method [221, 222] was shown to provide a computationally feasible route for calculating accurate temperature-dependent band gaps and other optoelectronic properties for a range of inorganic oxide and halide perovskites in [223].

4.2. Optical excitations in halide perovskites

Experimental optical absorption spectra of ABX_3 halide perovskites display a sharp resonance at the onset of absorption, which is consistent with the formation of a bound exciton [224–227] (see figure 3). The lineshape of the optical absorption spectrum of $MAPbI_3$ is described with very good accuracy by the Elliott model for optical absorption [228]. This approximation has been successfully used to extract key quantities, such as QP band gaps and exciton binding energies from optical absorption spectra measured on high quality thin films [225, 227, 229]. This is largely due to the parabolic and isotropic band edges and the weak binding energy of the excitons that characterize this halide perovskite family [230].

Excitons in halide perovskites have binding energies below 100 meV, increasing as the size of the halogen atom decreases [161, 225, 232]. These weak binding energies are consistent with the standard Wannier–Mott model for excitons, which relates the binding energy, E_B, the dielectric constant, ε, and the reduced effective mass, μ, of a semiconductor through a very simple formula, $E_B = \mu/(2\varepsilon^2)$, as expressed in atomic units. The Wannier–Mott model is frequently used to extract the exciton binding energy from raw experimental data, for example from the energy difference between the 1*s* and 2*s* excited states, when these can be resolved in experiments [225].

In addition to the exciton binding energies, optical measurements under high magnetic fields also allow an accurate measurement of the exciton reduced effective mass, μ. This quantity can be extracted from the resolved Landau levels at high magnetic fields, $\mu = B/\omega_c$, where ω_c is the cyclotron frequency measured as the difference between two consecutive Landau levels, and B is the magnitude of the magnetic field [225]. Interestingly, in the case of $MAPbI_3$, applying the hydrogen model formula in conjunction with the measured reduced effective mass (0.11 m_e) and exciton binding energy (16 meV) [225], yields a corresponding *effective* dielectric constant of approximately 9.5 [225], larger than the high-frequency (electronic) dielectric constant of 5.5–6.5 and lower than the low-frequency (static) dielectric constant of approximately 30 [230, 233]. This apparent inconsistency was associated with a possible contribution to the dielectric screening by IR active phonons [162].

Exciton binding energies and optical absorption spectra are very challenging to calculate within state-of-the-art *GW*+BSE for organic-inorganic halide perovskites, and only a handful of studies have reported these calculations in the literature [140, 161, 162, 234]. Adding to the complexities related to structural and starting-point dependence of QP band gaps discussed in the previous section, the dispersion of the conduction and valence band edges in halide perovskites yields a difficult convergence for the exciton binding energy [140, 161]. The situation is very similar to the case of GaAs, for which the exciton binding energy of 4 meV is obtained only when the reciprocal space is sampled by more than 1 million points [150].

Unlike GaAs, however, ABX_3 halide perovskites unit cells consist of more atoms, and spin–orbit coupling is required in order to accurately resolve the conduction and valence band topology, making the **k**-point convergence a challenging computational bottleneck. Refs [140, 162] overcame this technical setback by using a model **q**-point dependence of the dielectric function [235] which neglects local field effects and allows to extrapolate exciton binding energy convergence to an infinitely dense grid. Alternatively, [161] used a similar approach as in [150], where the electron–hole interaction kernel is evaluated on a dense grid of **k**-points via an interpolation scheme [149], and a patched-sampling scheme is used to selectively sample this grid in the region of reciprocal space where the exciton is most localized [149, 236]. Regardless of the scheme used, [140, 161, 162, 237] independently calculated exciton binding energies for ABX_3 halide perovskites overestimated experimental measurements by a factor of 2 to 3, and attributed this result to the absence of phonon effects in standard GW+BSE calculations.

Umari *et al* [162] proposed that the overestimation of the first-principles exciton binding energies with respect to experiment is due to the absence of phonon-screening effects and introduced a model dielectric function that accounts for additional screening due to IR active phonon modes. Using this model, reference [162] showed that the exciton binding energy can be reduced by up to a factor of 2, achieving almost perfect agreement with experiment for $MAPbI_3$, and slightly overestimating values for other halide perovskites such as $CsPbI_3$. Recently, reference [161] generalized the BSE to include phonon-screening effects from first principles, and showed that phonon-screening corrections are significant for ABX_3 halide perovskites, but not as large as previously estimated, accounting for up to 20% of the difference between experimental and standard BSE calculations. Moreover, reference [161] showed that phonon-screening effects are important for computing exciton binding energies beyond halide perovskites, and can be significant in semiconductors and insulators across a variety of chemistries.

While phonon-screening effects can significantly reduce the exciton binding energy [161], the remaining missing physics in this picture resides with the nature of the individual photoexcited QPs bound by the Coulomb interaction, approximated as bare electrons and holes in standard theory, but generally dressed via the electron–phonon interaction into electron and hole polarons [169]. Polaronic effects have an important contribution to the properties of excitons in semiconductors and insulators [238–240]. Several models based on parabolic electronic bands and dispersionless single-mode polar phonons have been proposed to account for this contribution [241–244]. Furthermore, recent theoretical advancements in the description of exciton polarons, and particularly of self-trapped excitons, are opening the route to new capabilities to understand polaronic effects in complex functional materials [238–240].

4.3. Electron–phonon interactions and polarons

Electron–phonon interactions and polarons underpin the majority of optoelectronic properties of organic-inorganic halide perovskites under operating conditions. For example, the temperature dependence of the PL broadening [245] and charge-carrier mobilities [246] have been directly linked to the nature of the interaction between charge carriers and ionic vibrations in this family of materials. Additionally, the reduced effective mass of excitons, measured from optical spectra under high magnetic fields has been linked to polaronic mass-enhancement effects in lead-halide perovskites [247]. These observations are consistent with several other experimental reports on the formation of large polarons in organic-inorganic ABX_3 halide perovskites [248].

As hetero-polar materials (i.e. materials with more than one ionic species in their chemical composition), organic-inorganic ABX_3 halide perovskites display long-range IR-active polar modes with characteristic frequencies between 15 and 30 meV, depending on chemical composition [161, 233]. Temperature-dependent measurements of the PL linewidth in comparison with direct calculations of the imaginary part of the electron–phonon self energy, confirm that electron–phonon coupling in lead-halide perovskites (see figure 4) is dominated by the long-range Fröhlich interaction [249] between longitudinal optical (LO) phonons and charge carriers, while scattering with acoustic phonons is effectively negligible [245]. A similar observation can be made for the temperature dependence of charge-carrier mobilities. In [170], first-principles calculations of electron and hole charge-carrier mobilities demonstrate that the dominant interaction between charge carriers and ionic vibrations is that corresponding to long-range LO phonons. Moreover, a simple model including coupling only with the highest lying LO mode appears to accurately capture the physics of phonon-limited charge-carrier mobilities and provides physical intuition for temperature dependent charge transport properties in halide perovskites (see figure 4) [170]. This model can be successfully employed to also reproduce experimentally measured trends of the dependence of charge-carrier mobility in mixed-halide perovskites, lending further validation to current interpretations of electron–phonon interactions in halide perovskites [250].

Polarons are charged QPs which describe the deformation of the crystal lattice upon the addition or removal of an electron [151]. Depending on the extent of this deformation across the crystal, polarons are

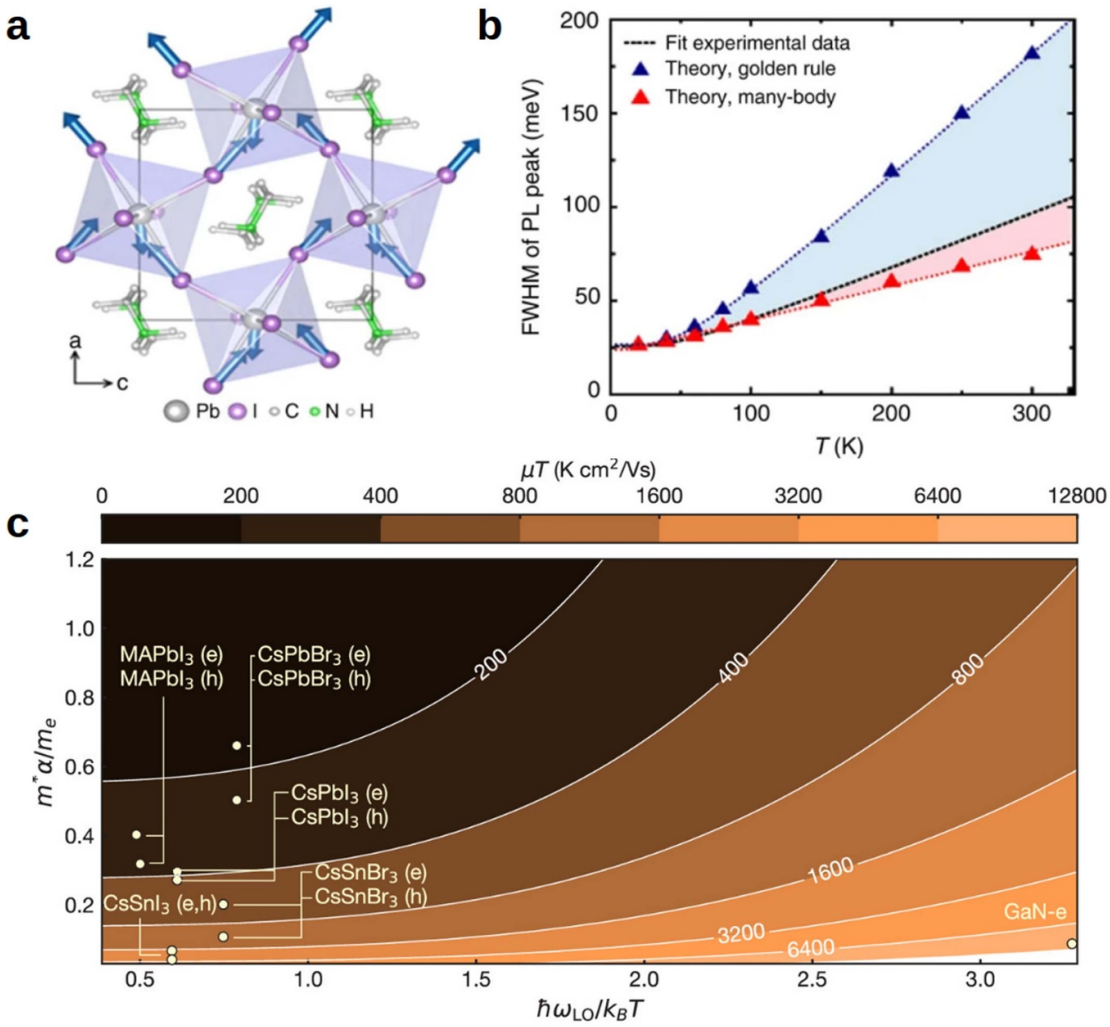

Figure 4. (a) Polyhedral model of $MAPbI_3$ with blue arrows depicting the LO vibrational mode giving rise to the PL line broadening. (b) PL line broadening as a function of temperature obtained from Brillouin–Wigner perturbation theory (red), the Fermi golden rule (blue), compared with experiment (black line) for $MAPbI_3$.(a) and (b) Reproduced from [245], with permission from Springer Nature. (c) Charge carrier mobility map as a function of the product of the effective mass (m^*) and the Fröhlich electron–phonon coupling strength α for halide perovskites, calculated using the model introduced in [200]. (c) Reprinted with permission from [200]. Copyright 2019 American Chemical Society.

typically categorized as 'large' (extending across several unit cells of the lattice) or 'small' (localized within approximately one unit cell). Standard methodologies based on DFT for computing polaron binding energies and estimating the sizes of polarons require modeling of very large supercells and are affected by the self-interaction error of DFT [251]. Therefore a deterministic approach to classifying the formation of large versus small polarons in complex systems like the halide perovskites can be challenging. A recently developed *ab initio* formalism allows the calculation of polaron binding energies and polaron wave functions within a framework similar to the BSE, and importantly by performing calculations in a single unit-cell [252, 253].

Large polarons occur due to long-range (Fröhlich) electron–phonon interactions, and are typical in the weak or intermediate coupling regime. In halide perovskites, large polaron formation has been linked to the phonon-limited charge-carrier mobility discussed above, and to the renormalization of the band gap and charge-carrier effective masses [247, 248, 254]. Schlipf *et al* [254] report computed electronic band structures renormalized by electron–phonon effects in $MAPbI_3$, and find an electron and hole effective masses enhancement of 28%. The same study used the computed mass-renormalization constant and the Feynman model for a large polaron [255] to estimate the polaron binding energy of 19–31 meV and a polaron radius of 62–81 Å (~20 PbI_6 octahedra) [254]. Several other computational studies using molecular-dynamics approaches have supported the hypothesis of large polaron formation in halide perovskites [256], and have studied the impact of polaron formation and lattice anharmonicity on the charge transport and recombination properties of halide perovskites [257, 258].

Formation of small polarons in halide perovskites is typically associated with disorder, or the existence of defects. References [259, 260] studied the formation and energy of small polarons via DFT, simulating the deformation of the lattice upon addition or removal of an electron in finite systems. Self-trapped polarons have been linked to fast non-radiative recombination, the presence of so-called 'color centers' [248], as well as to the photoinduced degradation of pristine and mixed-chemistry halide perovskites [261].

5. Beyond standard ABX_3 perovskites

5.1. Halide perovskites with mixed compositions

The ability to tune the band gap via total or partial chemical substitution of the A, B and X components is a highly attractive property of the ABX_3 halide perovskites. Partial mixing of two, three and even four cations has been used to improve the stability of halide perovskites against light- and moisture-driven degradation and halide segregation [262–265]. On the other hand, mixed-metal and mixed-halide compositions have been intensely explored as a route to optimize the efficiency of single-junction perovskite solar cells [266], as well as develop highly efficient silicon-perovskite [267] or perovskite-perovskite tandem solar cells [268]. Partial mixing of metal and halogen atoms facilitates a fine-tuning of the band gap between the extreme points corresponding to the pristine structures, however the trend is non-linear with respect to the mixing concentration, exhibiting a so-called band gap 'bowing' effect [269, 270]. This non-linear and even non-monotonous dependence of the band gap on the mixing concentration appears to be particularly prominent for mixed Pb-Sn perovskites [268, 271], while it is less pronounced (although still present) for mixed-halide perovskites [272–275].

Halide perovskites with mixed A-, B- and X- compositions pose great challenges to standard first-principles methods relying on periodic boundary conditions, as they require, in principle, a simultaneous treatment of both compositional and structural disorder, and involve in practice a large number of calculations on very large supercells [276–280]. The virtual crystal approximation (VCA) [281] is a useful alternative approach to studying crystalline systems involving mixed species, and it is particularly suitable for applications to halide perovskites. The premise of this approximation is that chemical mixing is uniform throughout the crystal, and that the impact of local structural distortions on the electronic structure properties can be neglected. Halide perovskites with mixed B- and X-site compositions have been studied within DFT [268, 282, 283], using both the VCA [281] or by simulating mixed compositions using large supercells [284]. DFT calculations employing the VCA successfully reproduced qualitative band gap trends for mixed-halide perovskites [282], as shown for example in figure 5(a). However calculations on mixed Pb-Sn systems with the VCA did not capture the bowing effect reported in experiments [268]. For the latter, the supercell approach was also used, successfully reproducing the experimental band-gap trend [268, 271], and indicating that local structural distortions of the Pb and Sn-centered octahedra may play an important role in the electronic structure of these mixed species, as illustrated in figures 5(b) and (c). On the other hand, it is not yet clear whether mixed Pb/Sn perovskites exhibit any long-range order of metal components, as it is generally assumed in computational modeling studies employing periodic boundary conditions [268]. More in-depth studies are needed to fully understand the impact of disorder in these compounds.

The problem becomes even more complicated from a theoretical point of view when mixed-cation compositions are considered, where often both compositional and rotational disorder must be accounted for. For example, DFT-based studies have revealed that cation mixing can decrease the activation energy of mobile halogen ions [285], and possibly induce significant distortions in the metal-halide network, suppressing octahedral tilting and inducing local symmetry breaking [286].

5.2. Double perovskites

The rapid rise of organic-inorganic lead-halide perovskites has been a great catalyst for theoretical and experimental efforts in materials design and discovery studies, mostly aiming to reveal whether there are any other halide perovskite materials that have equally impressive optoelectronic properties as the lead-halides [7, 27]. These efforts have recently materialized in the design and (re-)discovery of three-dimensional halide double perovskites which formally replace divalent Pb by a heterovalent pair of B-site metal ions [28, 287–292] or by a tetravalent ion such as Sn^{4+} [293] or Pd^{4+} [294] and a vacancy (see section 2). Developing an in-depth atomistic understanding of the optoelectronic properties of these materials is crucial for their deployment to suitable applications, and first-principles computational modeling techniques described in this review have been playing a fundamental role in this context.

First-principles calculations within semi-local and hybrid DFT, as well as MBPT confirm that the electronic band structure of halide double perovskites is drastically impacted by the chemical composition at the B and B′ atomic sites. Halide double perovskites based on pnictogen and noble metals (Cs_2AgBiX_6, Cs_2AgSbX_6 with X = Cl, Br) exhibit indirect band gaps in the visible range, with anisotropic valence and

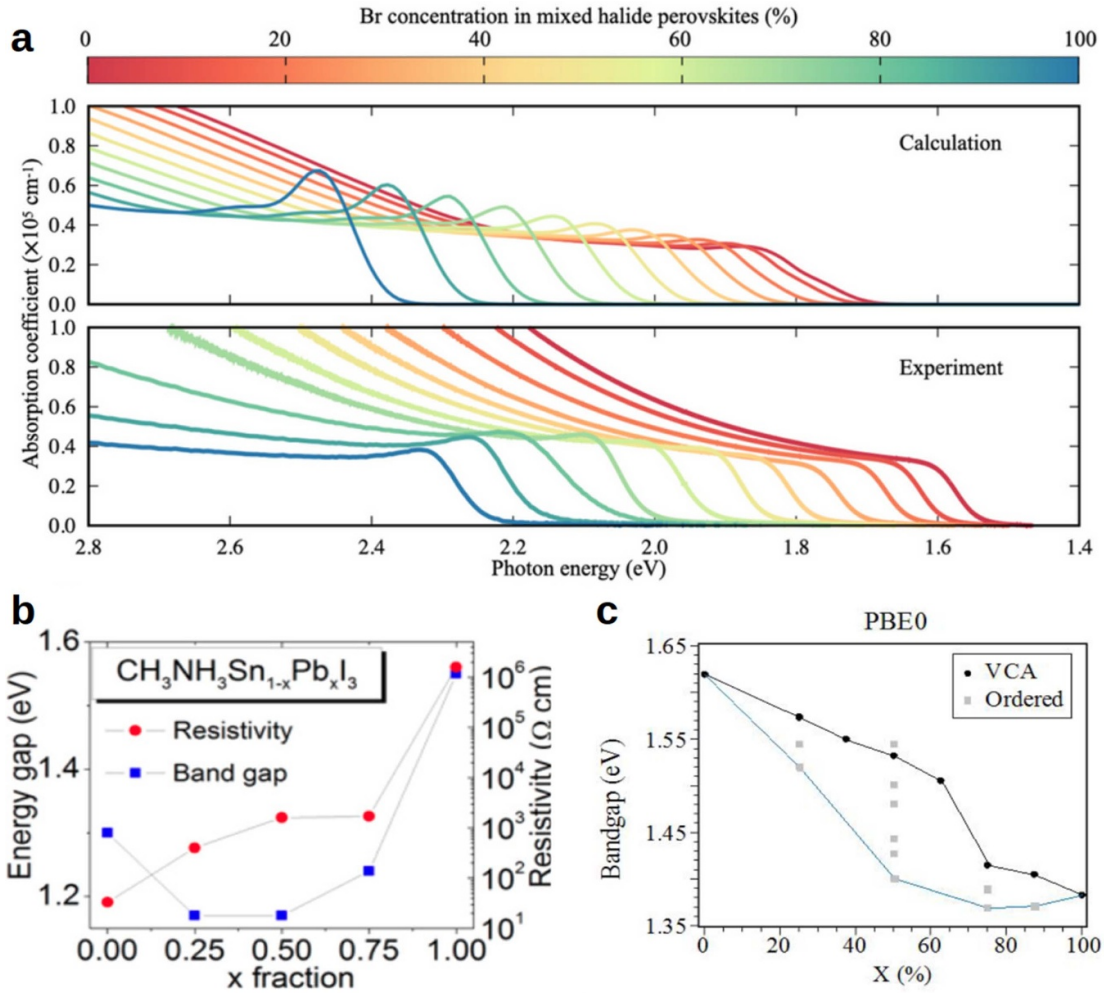

Figure 5. (a) Comparison of computed and experimental optical absorption spectra for mixed iodide-bromide perovskites, with calculations performed within the *GW*+BSE framework and using the virtual crystal approximation (VCA). (a) Reprinted with permission from [250]. Copyright 2022 American Chemical Society. (b) Measurements of the dependence of band gap and resistivity on the Pb-Sn mixing concentration. (b) Reprinted with permission from [271]. Copyright 2014 American Chemical Society. (c) Computed dependence of the band gap as a function of Pb-Sn mixing concentration using the VCA and ordered supercells. (c) From [268]. Reprinted with permission from AAAS.

conduction band edges [289, 290, 296]. Cs_2AgBX_6 (with B = In or Tl [291, 292]) and vacancy-ordered double perovskites Cs_2BX_6 (B = Sn, Pd [294, 297]) exhibit a direct gap with a disperse and isotropic conduction band and a flat anisotropic valence band edge. To understand these qualitative differences in the character of the electronic band edges, [295] developed a model based on linear combinations of atomic orbitals (LCAO) using symmetry-adapted linear combinations (SALCs) of halide orbitals to connect the electronic structure and symmetry of the atomic orbitals within BX_6 octahedral units to the character and dispersion of the band edges. For example, as shown in figure 6, the valence band top at the X-point in $Cs_2AgBiBr_6$ is found by locating the Bloch wave which corresponds to the maximum number of anti-bonding interactions between halide SALCs and metal Ag-*d* and Bi-*s* orbitals, while the conduction band minima at the L-point originates from Ag-*s* bonding orbitals. This type of analysis successfully predicts the character of almost all known halide double perovskites semiconductors without the need for first-principles calculations, and can be a powerful tool for materials design, especially given that the number of possible chemical compositions amenable for the double perovskite structure is of more than 90 000 [28, 29]. Quantitative predictions of double perovskite band gaps based on generalized Kohn–Sham DFT or MBPT are complicated by factors similar to those discussed in sections 4.1.1 and 4.1.2 for single perovskites, i.e. a consistent choice of structural model, the choice of PP, details of implementation, and the starting-point dependence of the G_0W_0 approach. References [112, 141] provide an overview of band gaps of a range of double perovskites using hybrid DFT, G_0W_0 constructed from semilocal and hybrid DFT starting points, and the meta-GGA TASK, respectively.

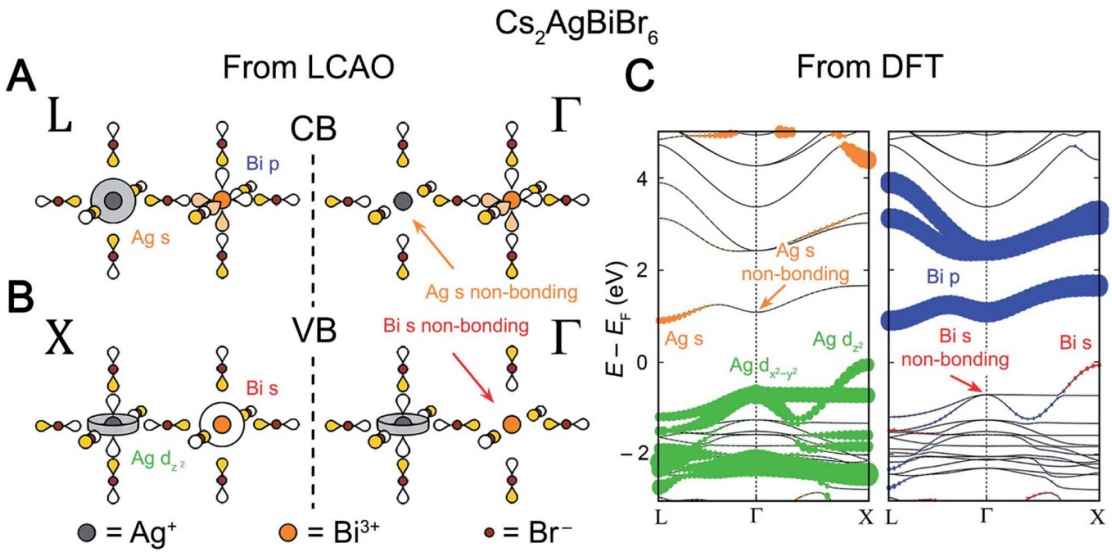

Figure 6. LCAO representations of (A) the conduction band (CB) at L and Γ and (B) the valence band (VB) at X and Γ for $Cs_2AgBiBr_6$, obtained using LCAO theory. Net nonbonding interactions between the halide SALCs and the metal s orbitals explain the missing Ag 5 s^0 (orange arrow) and Bi 6 s^2 (red arrow) orbital contributions at Γ at the CB and VB, respectively. Colored and empty lobes represent positive and negative phases, respectively. (C) Band structure of the double perovskite $Cs_2AgBiBr_6$ computed using DFT, showing an indirect gap from X to L. The band structure is shown in duplicate and the orbital contributions of the B-site atoms (Ag and Bi) are given in color with the dot size proportional to the size of the orbital contribution. Bromine contributions are present but not shown. Reproduced from [295] with permission from the Royal Society of Chemistry.

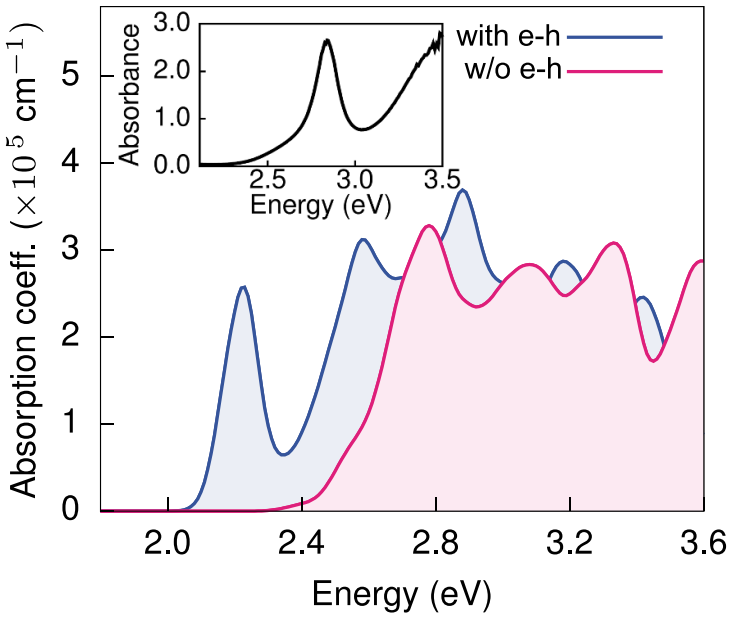

Figure 7. Calculated optical absorption spectrum of $Cs_2AgBiBr_6$ with (blue) and without (pink) electron-hole interactions, replotted here with permission by the authors of reference [296]. The inset uses experimental data from [298] with permission by the authors of [298].

Halide double perovskites display somewhat counter-intuitive features in their measured optical absorption spectra to what is expected from their electronic band structure. The optical absorption spectrum of $Cs_2AgBiBr_6$ exhibits a slow rise in the absorption coefficient, consistent with an indirect band gap, followed by a sharp peak approximately 0.5 eV above the onset [298]. Recent first-principles studies based on *GW*+BSE [296, 299] confirmed that this peak is a resonant excitonic feature emerging from the direct band-to-band transition at the X-point in the Brillouin zone, with a binding energy exceeding 170 meV [296] (see figure 7). In addition, [296] also revealed that strongly bound excitons with binding energies of up to 400 meV are an intrinsic feature of the pnictogen-noble metal halide double perovskite family, which originates from the anisotropy of the electronic band edges and the dielectric function [300, 301].

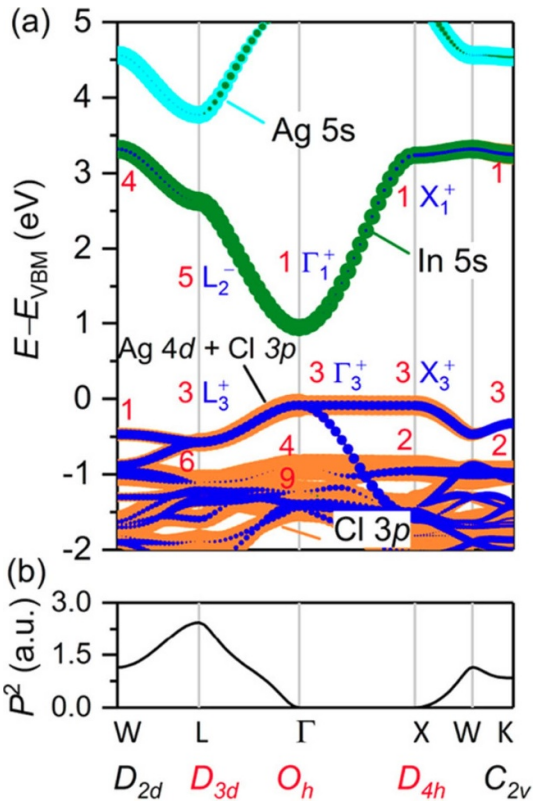

Figure 8. (a) Band structure of $Cs_2InAgCl_6$ with the overlayed orbital contributions for individual atomic compositions. (b) Optical matrix elements corresponding to band-to-band transitions computed and plotted along the high symmetry path. Reprinted with permission from [303]. Copyright 2017 American Chemical Society.

The absorption spectrum of $Cs_2AgInCl_6$ is also atypical, in that it displays a slow rise in the optical absorption coefficient at the onset [291, 292, 300, 302] instead of the sharp increase expected from direct band gap semiconductors. In addition, several of the lowest lying bound excitonic states calculated from *GW*+BSE are not optically active [302], and originate in parity-forbidden optical transitions from the valence to the conduction band edges [303] (see figure 8). Reference [302] showed that by alloying Ag with Na, the parity-forbidden symmetry of these transition can be broken, thereby allowing activation of these excitonic states in mixed Ag/Na compounds. Notably, a similar absorption spectrum lineshape to $Cs_2AgInCl_6$ has also been observed in the vacancy ordered double perovskite Cs_2PdBr_6 [294], given the resemblance in the band edge topology of these two systems.

Similar to the mixed B-site halide perovskites described in section 5.1, B-site alloying is a powerful tool for material design in halide double perovskites too, and has been studied most widely for the double perovskite $Cs_2AgBiBr_6$. Using a combination of experimental techniques and DFT calculations, it was shown that dilute alloying of $Cs_2AgBiBr_6$ with Tl^{3+} decreases the band gap of $Cs_6AgBiBr_6$ by 0.5 eV due to the formation of an isolated impurity band derived from Tl 6*s* orbitals below the host lattice's conduction band bottom [304]. Fully replacing Bi^{3+} by Tl^{3+} leads to a halide double perovskite with a band gap of less than 1 eV, as confirmed by *GW* calculations. Additionally, tight-binding modelling showed that the unusually small band gaps of Cs_2AgTlX_6 (X = Br, Cl) as compared to other bromide and chloride perovskites are due to the symmetry- and energy-aligned B and B' site orbitals contributing to the band edges of these compounds [292]. Similar effects have been achieved using dilute heterovalent alloying, for example of $Cs_2AgBiBr_6$ with Sn and $Cs_2AgInCl_6$ with Cu [305, 306]. Another promising route for functionalizing halide double perovskites is B-site mixing with transition metals leading to spin-polarized electronic structures and the possibility of magnetic ordering [307–309].

An ongoing open question for the optoelectronic properties of halide double perovskites such as Cs_2AgBiX_6 and $Cs_2AgInCl_6$ is the origin of the large red-shift of the PL spectrum as compared to the onset of the optical absorption [291, 310], which exceeds 0.5 eV for $Cs_2AgBiBr_6$ and 1.2 eV for $Cs_2AgInCl_6$. The G_0W_0 QP indirect band gap of 1.9 eV computed for $Cs_2AgBiBr_6$ in [290] was in very good agreement with the peak position of the PL spectrum, prompting a tentative assignment of the broad PL peak to indirect recombination [290]. However, given the sensitivity to the mean-field starting points of QP band gaps [141], it is more likely that this assignment is coincidental. Instead, recent experimental studies propose that the

red-shifted broad PL peak is due to self-trapped charge carriers diffusing to color centers [311, 312]; further first-principles studies of electron–phonon interactions and polaronic properties of $Cs_2AgBiBr_6$ may elucidate the atomistic picture of this process. In the case of $Cs_2AgInCl_6$, the QP band gap also exhibits a strong dependence on the starting point, as shown in a recent first-principles study [313], with values ranging from 1.9 to 3.4 eV depending on the starting point (LDA vs PBE), implementation of self-consistency and inclusion of semicore states. Taking into account that the QP band gap is renormalized by 0.2 eV [313] by the electron–phonon interaction and including the effect of electron–hole interactions (with an exciton binding energy of 0.25 eV) [302], the onset of the optical absorption spectrum can be assigned to optical absorption at the band edges. On the other hand, neither electron–phonon nor electron–hole interactions can explain the PL peak centered at 2 eV. Alternative explanations include the formation of strongly bound polarons and/or self trapped excitons [313], or defect-induced emission. While neither possibilities have been investigated thus far in first-principles studies, a recent first-principles study of self-trapped polarons in closely related Cs_2ZrBr_6 [238] point to the possibility that new theoretical developments for understanding exciton-polarons may provide the route to explaining the large shift between the optical absorption onset and the PL peak in some of the members of this materials family.

5.3. Quasi-2D halide perovskites and other perovskite-like materials

Understanding optoelectronic properties of quasi-2D halide perovskites using first-principles techniques is a challenging task, not least because of the chemical heterogeneity (inherited in part from the 3D perovskites) and structural complexity of this family of materials [34], as introduced in section 2.3. The optoelectronic properties of quasi-2D halide perovskites inherit the broad tunability of optoelectronic properties via the chemistry of the inorganic layer of their 3D counterparts [17, 314], an attractive feature for design of optoelectronic devices. Additionally, and by contrast with their 3D congeners, the organic cation in layered halide perovskites plays a much more significant role in the photophysics of these complex materials [36, 315–321]. Quasi-2D halide perovskites are significantly more chemically versatile than their 3D counterparts. This is largely due to the seemingly endless options for organic cations that can be incorporated between the metal-halide layers [34, 322] which in turn leads to a large array of possible structural configurations (as discussed in section 2.3). To a great extent, it is fair to say that more quasi-2D perovskites are synthesized than we can develop fundamental understanding for. In this context, development of chemical intuition for their optoelectronic properties is of great importance for guiding future materials design.

First-principles calculations of the electronic structure of layered perovskites based on DFT or semi-empirical tight-binding modeling reveal structure property relationships which are both inherited from 3D perovskites (such as the modulation of the band gap and effective mass via octahedral tilting [323, 324]) and unique to the quasi-2D systems (for example the control of dimensional confinement within the inorganic layer by combining face and corner-sharing octahedra [40, 325]). Furthermore, DFT calculations reveal interesting quantum-confinement effects on the electronic band structure of layered perovskites, depending on the metal type. While layered halide perovskites based on Pb and Sn maintain the direct nature of the band gap regardless of the thickness of the inorganic layer [40, 323], layered double perovskites feature indirect-to-direct and direct-to-indirect band gap transitions depending on B and B' site orbital composition when thinned down to the monolayer limit, bearing similarities with monolayer transition metal dichalcogenides [38, 39]. These changes in band-gap character can be explained using an LCAO model similar to that previously used for 3D double perovskites [295] adapted to the 2D translational symmetry of these layered materials and are predicted to be prevalent in layered perovskites with band edges derived from metal-d states or a VBM without metal-orbital contributions [326].

Layered organic-inorganic halide perovskites are often regarded as natural quantum-well superstructures [327], which draws the focus on understanding the dielectric and quantum confinement effects in these systems. Blancon *et al* [328] used the generalized Keldysh theory alongside key quantities extracted from DFT calculations to develop a model to establish that the variation of the exciton binding energy in quasi-2D halide perovskites with increasing thickness of the inorganic layers is a combined quantum and dielectric confinement effect. In a separate study, reference [329] developed a tight-binding-based approach to apply the BSE equation to Ruddlesden-Popper layered perovskites with increasing inorganic layer thickness and revealed that 1*s* and 2*s* excitonic states in these complex structures do not follow trends dictated by the 2D hydrogenic model. Following results from this work, reference [327] further developed this methodology to compute trion and biexciton binding energies between 30 and 50 meV, which remarkably do not change significantly upon exfoliation of a single layer (unlike the exciton binding energy which nearly doubles according to these calculations).

Only a handful of first-principles calculations of optical excitations in quasi-2D halide perovskites have so far been reported in the literature [317, 318, 320, 330–332], owing to the complexity of these organic-inorganic semiconductors. Molina-Sánchez [330] relied on the observation that organic cations do

not contribute single-particle states at the band edges, and used a simplified model structure of a layered perovskite whereby the organic cations are replaced by Cs to compute the optical absorption spectrum and underlying excitonic states for a perovskite monolayer. The exciton binding energy reported for this bromide-based model system is of up to 600 meV. Filip *et al* [331] used *GW*+BSE to delineate the role of the organic cation in Ruddlesden-Popper perovskites, via a comparative study of optical excitation energies and QP band gaps computed for both model and real experimental structures with and without (i.e. replaced by Cs) organic cations of increasing sizes. Calculations in [331] reveal and quantify the contribution of the organic cations to the dielectric screening of the bulk layered perovskite, which counteracts quantum confinement effects and reduces the exciton binding energy sometimes by several hundreds of meV [331].

In addition to dielectric screening, organic cations determine the separation between inorganic lead-halide layers in layered perovskites, which can be reduced in some cases to close enough distances that peripheral halogen anion orbitals can interact (especially in Dion–Jacobson perovskites) [332]. Due to this interaction, the single layer confinement of the lowest energy exciton, usually observed in the Ruddelsden–Popper layered perovskites, can be overcome, and the exciton wavefunction becomes delocalized across several neighboring layers [332]. These examples demonstrate, that the organic cations can be used as an additional tuning vehicle for the dielectric properties, and implicitly the QP band gap and exciton binding energies of quasi-2D halide perovskites. Finally, it is worth mentioning that while the electronic states localized on the organic cation are usually assumed to have energies that are far below or above the band edges, there have been several examples of layered perovskites demonstrated in which organic cations feature electronic states either within the band gap or close to the band edges [318, 333, 334], and thereby possibly facilitating charge transfer between the perovskite and organic layers.

In addition to lead-based layered perovskites of the Ruddlesden–Popper series, *GW*+BSE studies of excitonic properties have also been reported for lead-free pnictogen-noble metal layered perovskites. References [299, 335] reported on the excitonic properties of Bi/Ag based layered double perovskites, which exhibit a strong out-of-plane optical response. Furthermore, [299] noted that instead of a decrease in the exciton binding energy with the increase in layer thickness, as expected for standard Ruddlesden–Popper series, such a trend does not appear to be so well defined in double perovskites. The atomistic origin of this observation remains to be clarified.

Despite the structural complexity of organic-inorganic quasi-two dimensional perovskites, thanks to state-of-the-art advances in the implementation of MBPT methods [336, 337] it is now possible to study photophysical properties of ever-more complex superstructures, including complex interfaces between perovskites and non-perovskites [338]. *GW*+BSE calculations of newly synthesized intergrowth hetero-structures including inorganic lead-bromide and lead-chloride perovskites and non-perovskite layers, reveal that chemical engineering of such hetero-interfaces may lead to yet another route to not only control the energy but also the delocalization of excitons in these superstructures [338].

Finally, first-principles studies have also been used to explore structures in which the corner-sharing connectivity of metal-halide octahedra is broken in more than one direction, such as the composition $A_3B_2X_9$ with B = Bi, Sb, or has a different periodicity, such as in the extended perovskite analogues, both introduced in section 2.4. The excitonic properties of $Cs_3Bi_2I_9$, a quasi-0D material, were reported in [339] and shown to be determined by the relatively flat, strongly spin–orbit split Bi-*p*-derived bands of this compound, resembling those of other Bi-containing perovskites. Qualitatively different excited states are expected for the extended perovskite analogues in which, contrary to other known perovskites, the conduction band is derived from electronic states associated with the molecular A-site [45, 49]. The excitonic properties of these complex organic-inorganic compounds are yet to be explored using first-principles techniques.

6. Summary, future work and challenges

In the previous sections we have attempted to outline the promises and challenges of first-principles calculations for halide perovskites due to the complex coupled electronic and structural dynamics of these materials. While a qualitative understanding can in many cases be reached based on standard approaches for semiconducting solids such as tight-binding models, as described in section 4.1.1, a quantitative description requires advanced first-principles numerical modelling techniques. The example of accurately predicting the band gaps of perovskites detailed in sections 4.1.2 and 4.1.3 shows that computationally demanding methods such as hybrid functional starting points for G_0W_0 calculations or self-consistency in the *GW* procedure combined with adequate methods for taking into account the effects of temperature are necessary to reach agreement with experiment for the broad range of halide perovskites covered in this review.

In the preceding discussion, we have mostly avoided the important topic of first-principles calculations of defects in halide perovskites. The study of how lattice impurities and point defects affect the electronic and excited-state structure of solids typically requires large supercells and well-established correction methods

for extrapolating defect formation energies and transition levels to the dilute or isolated defect limit [340]. Such techniques have been employed widely for calculating defect levels in halide perovskites and we refer the reader to a review by Meggiolaro and De Angelis for more detailed information about the successes and pitfalls of such calculations [341]. One clear limitation of standard computational frameworks for defect calculations of perovskites is that they are based on static structures. Such calculations do not take into account the temperature-dependent structural dynamics of the perovskite lattice, which have been shown to be strongly anharmonic for some perovskites [342–345]. The impact of structural dynamics on defect transition levels was shown in large-scale first-principles molecular dynamics calculations of $CsPbBr_3$ [346], raising questions about the validity of static structural defect models for strongly anharmonic halide perovskites at elevated temperatures [346]. In addition, electron–hole interactions may also play an important role, as it was shown for example in studies of monolayer transition metal dichalcogenides [347], gallium nitride [348], and monolayer germanium selenide [166]. For halide perovskite, these calculations remain computationally challenging requiring the use of supercells with hundreds of atoms on top of the challenges described in sections 4.1.2 and 4.1.3.

Further functionalization of halide perovskites has led to an extension of the perovskite family to the materials touched upon in section 5.3 and larger and larger structures, including complex interfaces and heterostructures. While such systems featuring hundreds of atoms were still out of reach for first-principles calculations just a couple of years ago, recent developments have allowed for excited-states calculations of systems of unprecedented size [336, 337]. At the same time, method development in the areas of quantum embedding [349–351], machine-learning approaches for excited states [352, 353], density functional development [354], and GPU-accelerated implementations of MBPT [355–357], also open up new avenues for the accurate calculation of optoelectronic properties of structurally and chemically complex halide perovskites at reduced computational cost. The challenge for the future will be to develop workflows which combine state-of-the-art methodologies in order to efficiently extract photophysical properties of complex and heterogeneous perovskites and perovskite-related materials under device operating conditions. As this broad materials family evolves from design hypothesis to synthesis to integration in functional devices, it is becoming evident that interweaving state-of-the-art computational modeling and experimental characterization workflows in collaborative and inter-disciplinary studies has the highest potential to drive future development of both practical devices and methodological advances.

Data availability statement

No new data were created or analysed in this study.

Acknowledgments

The authors would like to gratefully acknowledge Dr Carla Verdi from the University of Queensland and Dr Jonah Haber from Stanford University for their critical reading and helpful suggestions for the presentation of this review article. LL acknowledges funding by the Dutch Research Council (NWO) through the Grants OCENW.M20.337 and VI.Vidi.223.072. MRF acknowledges funding support from the Engineering and Physical Sciences Research Council (EPSRC) and the Oxford University Press John Fell Fund.

ORCID iDs

Marina R Filip https://orcid.org/0000-0003-2925-172X
Linn Leppert https://orcid.org/0000-0002-4361-4382

References

[1] Lee M M, Teuscher J, Miyasaka T, Murakami T N and Snaith H J 2012 *Science* **338** 643
[2] Kitazawa N, Watanabe Y and Nakamura Y 2002 *J. Mater. Sci.* **7** 3585–7
[3] Diekmann J *et al* 2021 *Solar RRL* **5** 2100219
[4] Zhu H, Miyata K, Fu Y, Wang J, Joshi P, Niesner D, Williams K W, Jin S and Zhu X-Y 2016 *Science* **353** 1409
[5] Yaffe O *et al* 2017 *Phys. Rev. Lett.* **118** 136001
[6] Guo Y, Yaffe O, Hull T D, Owen J S, Reichman D R and Brus L E 2019 *Nat. Commun.* **10** 1175
[7] Brandt R E, Stevanovi V, Ginley D S and Buonassisi T 2015 *MRS Commun.* **5** 265–75
[8] Walsh A and Zunger A 2017 *Nat. Mater.* **16** 964–7
[9] Nayak P K, Mahesh S, Snaith H J and Cahen D 2019 *Nat. Rev. Mater.* **4** 269–85
[10] Al-Ashouri A *et al* 2020 *Science* **370** 1300–9
[11] Sutherland B R and Sargent E H 2016 *Nat. Photon.* **10** 295–302
[12] Worku M, Ben-Akacha A, Blessed Shonde T, Liu H and Ma B 2021 *Small Sci.* **1** 2000072
[13] Wei H and Huang J 2019 *Nat. Commun.* **10** 1066

[14] Liu F, Wu R, Wei J, Nie W, Mohite A D, Brovelli S, Manna L and Li H 2022 *ACS Energy Lett.* **7** 1066–85
[15] Huang H, Weng B, Zhang H, Lai F, Long J, Hofkens J, Douthwaite R E, Steele J A and Roeffaers M B J 2022 *J. Phys. Chem. Lett.* **13** 25–41
[16] McMillon-Brown L, Luther J M and Peshek T J 2022 *ACS Energy Lett.* **7** 1040–2
[17] Saparov B and Mitzi D B 2016 *Chem. Rev.* **116** 4558–96
[18] Mitzi D B 2019 *Chem. Rev.* **119** 3033–5
[19] Rondinelli J M and Coh S 2011 *Phys. Rev. Lett.* **106** 235502
[20] Spaldin N A and Ramesh R 2019 *Nat. Mater.* **18** 203–12
[21] Rabe K M, Walker F J, Shin Y J and Ahn C H 2022 *Adv. Electron. Mater.* **8** 2200146
[22] Goldschmidt V M 1926 *Naturwissenschaften* **14** 477–85
[23] Kieslich G, Sun S and Cheetham A K 2015 *Chem. Sci.* **6** 3430–3
[24] Poglitsch A and Weber D 1987 *J. Chem. Phys.* **87** 6373–8
[25] Glazer A M 1972 *Acta Crystallogr.* B **28** 3384–92
[26] Cross C W and Hillebrand W F 1883 *Am. J. Sci.* **s3–26** 271–94
[27] Wolf N R, Connor B A, Slavney A H and Karunadasa H I 2021 *Ang. Chem. Int. Ed.* **60** 16264–78
[28] Faber F A, Lindmaa A, Von Lilienfeld O A and Armiento R 2016 *Phys. Rev. Lett.* **117** 135502
[29] Filip M R and Giustino F 2018 *Proc. Natl Acad. Sci.* **115** 5397–402
[30] Igbari F, Wang Z K and Liao L S 2019 *Adv. Energy Mater.* **9** 1803150
[31] Ghosh S, Shankar H and Kar P 2022 *Mater. Adv.* **3** 3742–65
[32] Ruddlesden S N and Popper P 1957 *Acta Crystallogr.* **10** 538–9
[33] Ruddlesden S N and Popper P 1958 *Acta Crystallogr.* **11** 54–55
[34] Smith M D, Crace E J, Jaffe A and Karunadasa H I 2018 *Ann. Rev. Mater. Res.* **48** 111–36
[35] Blancon J C, Even J, Stoumpos C C, Kanatzidis M G and Mohite A D 2020 *Nat. Nanotechnol.* **15** 969–85
[36] Smith I C, Smith M D, Jaffe A, Lin Y and Karunadasa H I 2017 *Chem. Mater.* **29** 1868–84
[37] Li J *et al* 2018 *J. Am. Chem. Soc.* **140** 11085–90
[38] Connor B A, Leppert L, Smith M D, Neaton J B and Karunadasa H I 2018 *J. Am. Chem. Soc.* **140** 5235–40
[39] Connor B A, Biega R I, Leppert L and Karunadasa H I 2020 *Chem. Sci.* **11** 7708–15
[40] Kamminga M E, Fang H H, Filip M R, Giustino F, Baas J, Blake G R, Loi M A and Palstra T T M 2016 *Chem. Mater.* **28** 4554–62
[41] Park B-W, Philippe B, Zhang X, Rensmo H, Boschloo G and Johansson E M J 2015 *Adv. Mater.* **27** 6806–13
[42] Lehner A J, Fabini D H, Evans H A, Hébert C-A, Smock S R, Hu J, Wang H, Zwanziger J W, Chabinyc M L and Seshadri R 2015 *Chem. Mater.* **27** 7137–48
[43] Giustino F and Snaith H J 2016 *ACS Energy Lett.* **1** 1233–40
[44] Bass K K, Estergreen L, Savory C N, Buckeridge J, Scanlon D O, Djurovich P I, Bradforth S E, Thompson M E and Melot B C 2017 *Inorg. Chem.* **56** 42–45
[45] Umeyama D, Leppert L, Connor B A, Manumpil M A, Neaton J B and Karunadasa H I 2020 *Ang. Chem. Int. Ed.* **59** 19087–94
[46] Zhang H-Y, Song X-J, Cheng H, Zeng Y-L, Zhang Y, Li P-F, Liao W-Q and Xiong R-G 2020 *J. Am. Chem. Soc.* **142** 4604–8
[47] Tang Y-Y, Liu Y-H, Peng H, Deng B-B, Cheng T-T and Hu Y-T 2020 *J. Am. Chem. Soc.* **142** 19698–704
[48] Li X, He Y, Kepenekian M, Guo P, Ke W, Even J, Katan C, Stoumpos C C, Schaller R D and Kanatzidis M G 2020 *J. Am. Chem. Soc.* **142** 6625–37
[49] Matheu R, Ke F, Breidenbach A, Wolf N, Lee Y, Liu Z, Leppert L, Lin Y and Karunadasa H 2022 *Ang. Chem. Int. Ed.* **61** e202202911
[50] Giannozzi P *et al* 2017 *J. Phys.: Condens. Matter* **29** 465901
[51] Kresse G and Hafner J 1993 *Phys. Rev.* B **47** 558–61
[52] Kresse G and Hafner J 1994 *J. Phys.: Condens. Matter* **6** 8245–57
[53] Kresse G and Furthmüller J 1996 *Phys. Rev.* B **54** 11169–86
[54] Deslippe J, Samsonidze G, Strubbe D A, Jain M, Cohen M L and Louie S G 2012 *Comput. Phys. Commun.* **183** 1269–89
[55] Barker B A, Deslippe J, Lischner J, Jain M, Yazyev O V, Strubbe D A and Louie S G 2022 *Phys. Rev.* B **106** 115127
[56] Marini A, Hogan C, Grüning M and Varsano D 2009 *Comput. Phys. Commun.* **180** 1392–403
[57] Perdew J P and Kurth S 1998 Density functionals for non-relativistic coulomb systems *Density Functionals: Theory and Applications: Proc. 10th Chris Engelbrecht Summer School in Theoretical Physics Held at Meerensee, Near Cape Town South Africa (19–29 January 1997) (Lecture Notes in Physics)* ed D Joubert (Springer) pp 8–59
[58] Capelle K 2006 *Braz. J. Phys.* **36** 1318
[59] Hohenberg P and Kohn W 1964 *Phys. Rev.* **136** B864
[60] Kohn W and Sham L J 1965 *Phys. Rev.* **385** A1133
[61] Giustino F 2014 *Materials Modelling Using Density Functioal Theory* (Oxford University Press)
[62] Seidl A, Görling A, Vogl P, Majewski J A and Levy M 1996 *Phys. Rev.* B **53** 3764–74
[63] Kümmel S and Kronik L 2008 *Rev. Mod. Phys.* **80** 3
[64] Baer R, Livshits E and Salzner U 2010 *Ann. Rev. Phys. Chem.* **61** 85
[65] Kraisler E 2020 *Isr. J. Chem.* **60** 805–22
[66] Ceperley D M and Alder B J 1980 *Phys. Rev. Lett.* **45** 566
[67] Vosko S H, Wilk L and Nusair M 1980 *Can. J. Phys.* **58** 1200–11
[68] Perdew J P and Zunger A 1981 *Phys. Rev.* B **23** 5048–79
[69] Perdew J P and Wang Y 1992 *Phys. Rev.* B **45** 13244
[70] Perdew J P, Burke K and Ernzerhof M 1996 *Phys. Rev. Lett.* **77** 3865–8
[71] Zhao Y and Truhlar D G 2006 *J. Chem. Phys.* **125** 194101
[72] Becke A D 1988 *Phys. Rev.* A **38** 3098–100
[73] Lee C, Yang W and Parr R 1988 *Phys. Rev.* B **37** 785
[74] Zhou L, Yan Q, Shinde A, Guevarra D, Newhouse P F, Becerra-Stasiewicz N, Chatman S M, Haber J A Neaton J B and Gregoire J M 2015 *Adv. Energy Mater.* **5** 1500968
[75] Filip M R and Giustino F 2015 *J. Phys. Chem.* C **120** 166–73
[76] Shinde A, Suram S K, Yan Q, Zhou L, Singh A K, Yu J, Persson K A, Neaton J B and Gregoire J M 2017 *ACS Energy Lett.* **2** 2307–12
[77] Jain A, Voznyy O and Sargent E H 2017 *J. Phys. Chem.* C **121** 7183
[78] Bartel C J, Sutton C, Goldsmith B R, Ouyang R, Musgrave C B, Ghiringhelli L M and Scheffler M 2019 *Sci. Adv.* **5** eaav0693
[79] Behler J and Parrinello M 2007 *Phys. Rev. Lett.* **98** 146401

[80] Behler J 2016 *J. Chem. Phys.* **145** 170901
[81] Artrith N, Urban A and Ceder G 2017 *Phys. Rev.* B **96** 014112
[82] Lu S, Zhou Q, Ouyang Y, Guo Y, Li Q and Wang J 2018 *Nat. Commun.* **9** 3405
[83] Jinnouchi R, Lahnsteiner J, Karsai F, Kresse G and Bokdam M 2019 *Phys. Rev. Lett.* **122** 225701
[84] Schmidt J, Marques M R, Botti S and Marques M A 2019 *npj Comput. Mater.* **5** 83
[85] Pickard C J 2022 *Phys. Rev.* B **106** 014102
[86] Mori-Sánchez P, Cohen A and Yang W 2008 *Phys. Rev. Lett.* **100** 146401
[87] Cohen A J, Mori-Sánchez P and Yang W 2008 *Science* **321** 792
[88] Dreuw A and Head-Gordon M 2004 *J. Am. Chem. Soc.* **126** 4007–16
[89] Perdew J P, Ernzerhof M and Burke K 1996 *J. Chem. Phys.* **105** 9982–5
[90] Karolewski A 2013 Charge transfer in extended donor-acceptor systems with density functional theory *Doctoral Thesis* University of Bayreuth
[91] Becke A D 1993 *J. Chem. Phys.* **98** 5648–52
[92] Levy M 1982 *Phys. Rev.* A **26** 1200
[93] Adamo C and Barone V 1999 *J. Chem. Phys.* **110** 6158
[94] Toulouse J, Colonna F and Savin A 2004 *Phys. Rev.* A **70** 062505
[95] Kronik L, Stein T, Refaely-Abramson S and Baer R 2012 *J. Chem. Theory Comput.* **8** 1515–31
[96] Iikura H, Tsuneda T, Yanai T and Hirao K 2001 *J. Chem. Phys.* **115** 3540–4
[97] Vydrov O A and Scuseria G E 2006 *J. Chem. Phys.* **125** 234109
[98] Peach M J G, Helgaker T, Sałek P, Keal T W, Lutnæs O B, Tozer D J and Handy N C 2006 *Phys. Chem. Chem. Phys.* **8** 558–62
[99] Livshits E and Baer R 2007 *Phys. Chem. Chem. Phys.* **9** 2932–41
[100] Cohen A J, Mori-Sánchez P and Yang W 2007 *J. Chem. Phys.* **126** 191109
[101] Chai J D and Head-Gordon M 2008 *J. Chem. Phys.* **128** 084106
[102] Stein T, Eisenberg H, Kronik L and Baer R 2010 *Phys. Rev. Lett.* **105** 266802
[103] Refaely-Abramson S, Sharifzadeh S, Govind N, Autschbach J, Neaton J B, Baer R and Kronik L 2012 *Phys. Rev. Lett.* **109** 226405
[104] Wing D, Haber J B, Noff R, Barker B, Egger D A, Ramasubramaniam A, Louie S G, Neaton J B and Kronik L 2019 *Phys. Rev. Mater.* **3** 064603
[105] Ramasubramaniam A, Wing D and Kronik L 2019 *Phys. Rev. Mater.* **3** 084007
[106] Wing D, Ohad G, Haber J B, Filip M R, Gant S E, Neaton J B and Kronik L 2021 *Proc. Natl Acad. Sci.* **118** e2104556118
[107] Ohad G, Gant S E, Wing D, Haber J B, Camarasa-Gómez M, Sagredo F, Filip M R, Neaton J B , Kronik L 2023 *Phys. Rev. Mater.* **7** 123803
[108] Ohad G, Wing D, Gant S E, Cohen A V, Haber J B, Sagredo F, Filip M R, Neaton J B and Kronik L 2022 *Phys. Rev. Mater.* **6** 104606
[109] Gant S E, Haber J B, Filip M R, Sagredo F, Wing D, Ohad G, Kronik L and Neaton J B 2022 *Phys. Rev. Mater.* **6** 053802
[110] Sun J, Ruzsinszky A and Perdew J 2015 *Phys. Rev. Lett.* **115** 036402
[111] Aschebrock T and Kümmel S 2019 *Phys. Rev. Res.* **1** 033082
[112] Lebeda T, Aschebrock T, Sun J, Leppert L and Kümmel S 2023 *Phys. Rev. Mater.* **7** 093803
[113] Görling A 1996 *Phys. Rev.* A **54** 3912
[114] Janak J F 1978 *Phys. Rev.* B **18** 7165
[115] Levy M, Perdew J P and Sahni V 1984 *Phys. Rev.* A **30** 2745
[116] Almbladh C O and von Barth U 1985 *Phys. Rev.* B **31** 3231
[117] Perdew J P, Parr R G, Levy M and Balduz J J L 1982 *Phys. Rev. Lett.* **4** 1691
[118] Perdew J P and Levy M 1983 *Phys. Rev. Lett.* **51** 1884
[119] Sham L J and Schlüter M 1983 *Phys. Rev. Lett.* **51** 1888
[120] Perdew J P *et al* 2017 *Proc. Natl Acad. Sci.* **114** 2801–6
[121] Hybertsen M S and Louie S G 1985 *Phys. Rev. Lett.* **55** 1418–21
[122] Blase X, Rubio A, Louie S G and Cohen M L 1995 *Phys. Rev.* B **51** 6868–75
[123] Gomez-Abal R, Li X, Scheffler M and Ambrosch-Draxl C 2008 *Phys. Rev. Lett.* **101** 106404
[124] Shih B-C, Xue Y, Zhang P, Cohen M L and Louie S G 2010 *Phys. Rev. Lett.* **105** 146401
[125] Qiu D Y, Da Jornada F H and Louie S G 2013 *Phys. Rev. Lett.* **111** 216805
[126] Klimes J, Kaltak M and Kresse G 2014 *Phys. Rev.* B **90** 075125
[127] Rangel T *et al* 2020 *Comput. Phys. Commun.* **255** 107242
[128] Golze D, Dvorak M and Rinke P 2019 *Front. Chem.* **7** 377
[129] Onida G, Reining L and Rubio A 2002 *Rev. Mod. Phys.* **74** 601
[130] Hybertsen M S and Louie S G 1986 *Phys. Rev.* B **34** 5390
[131] Fuchs F, Furthmüller J, Bechstedt F, Shishkin M and Kresse G 2007 *Phys. Rev.* B **76** 115109
[132] Adler S L 1962 *Phys. Rev.* **126** 413
[133] Wiser N 1963 *Phys. Rev.* **129** 62
[134] Godby R W and Needs R J 1989 *Phys. Rev. Lett.* **62** 1169
[135] Lischner J, Pálsson G K, Vigil-Fowler D, Nemsak S, Avila J, Asensio M C, Fadley C S and Louie S G 2015 *Phys. Rev.* B **91** 205113
[136] Caruso F, Lambert H and Giustino F 2015 *Phys. Rev. Lett.* **114** 146404
[137] Larson P, Dvorak M and Wu Z 2013 *Phys. Rev.* B **88** 125205
[138] Brivio F, Walker A B and Walsh A 2013 *APL Mater.* **1** 042111
[139] Filip M R and Giustino F 2014 *Phys. Rev.* B **90** 245145
[140] Bokdam M, Sander T, Stroppa A, Picozzi S, Sarma D D, Franchini C and Kresse G 2016 *Sci. Rep.* **6** 28618
[141] Leppert L, Rangel T and Neaton J B 2019 *Phys. Rev. Mater.* **3** 103803
[142] Shishkin M and Kresse G 2007 *Phys. Rev.* B **75** 235102
[143] van Schilfgaarde M, Kotani T and Faleev S 2006 *Phys. Rev. Lett.* **96** 226402
[144] Kotani T, van Schilfgaarde M, Faleev S and van Schilfgaarde M 2007 *Phys. Rev.* B **76** 165106
[145] Grumet M, Liu P, Kaltak M, Klimeš J and Kresse G 2018 *Phys. Rev.* B **98** 155143
[146] Wiktor J, Rothlisberger U and Pasquarello A 2017 *J. Phys. Chem. Lett.* **8** 5507–12
[147] Gonze X *et al* 2020 *Comput. Phys. Commun.* **248** 107042
[148] Strinati G 1988 *Riv. Nuov. Cim.* **11** 1–86
[149] Rohlfing M and Louie S G 1998 *Phys. Rev. Lett.* **81** 2312–5

[150] Rohlfing M and Louie S G 2000 *Phys. Rev.* B **62** 4927
[151] Cohen M L and Louie S G 2016 *Fundamentals of Condensed Matter Physics* (Cambridge University Press)
[152] Refaely-Abramson S, da Jornada F H, Louie S G and Neaton J B 2017 *Phys. Rev. Lett.* **119** 267401
[153] Antonius G and Louie S G 2022 *Phys. Rev.* B **105** 085111
[154] Qiu D Y, Cohen G, Novichkova D and Refaely-Abramson S 2021 *Nano Lett.* **21** 7644–50
[155] Haber J B, Qiu D Y, da Jornada F H and Neaton J B 2023 *Phys. Rev.* B **108** 125118
[156] Chan Y H, Haber J B, Naik M H, Neaton J B, Qiu D Y and Louie S G 2023 *Nano Lett.* **23** 3971–7
[157] Chen H Y, Sangalli D and Bernardi M 2020 *Phys. Rev. Lett.* **125** 107401
[158] Folie B D, Haber J B, Refaely-Abramson S, Neaton J B and Ginsberg N S 2018 *J. Am. Chem. Soc.* **140** 2326–35
[159] Spataru C D, Ismail-Beigi S, Benedict L X and Louie S G 2004 *Phys. Rev. Lett.* **92** 077403
[160] Spataru C D and Léonard F 2010 *Phys. Rev. Lett.* **104** 177402
[161] Filip M R, Haber J B and Neaton J B 2021 *Phys. Rev. Lett.* **127** 067401
[162] Umari P, Mosconi E and De Angelis F 2018 *J. Phys. Chem. Lett.* **9** 620–7
[163] Adamska L and Umari P 2021 *Phys. Rev.* B **103** 075201
[164] Alvertis A M, Haber J B, Li Z, Coveney J N, Louie S G, Filip M R and Neaton J B 2023 arXiv:2312.03841
[165] Sharifzadeh S, Darancet P, Kronik L and Neaton J B 2013 *J. Phys. Chem. Lett.* **4** 2197
[166] Cohen A, Lewis D K, Huang T and Sharifzadeh S 2020 *Phys. Rev. Mater.* **4** 076002
[167] Arora A *et al* 2017 *Nat. Commun.* **8** 639
[168] Naik M H *et al* 2022 *Nature* **609** 52–57
[169] Giustino F 2016 *Rev. Mod. Phys.* **89** 1–64
[170] Poncé S, Margine E R and Giustino F 2018 *Phys. Rev.* B **97** 121201
[171] Pizzi G *et al* 2020 *J. Phys.: Condens. Matter* **32** 165902
[172] Marzari N, Mostofi A A, Yates J R, Souza I and Vanderbilt D 2012 *Rev. Mod. Phys.* **84** 1419–75
[173] Mostofi A A, Yates J R, Pizzi G, Lee Y-S, Souza I, Vanderbilt D and Marzari N 2014 *Comput. Phys. Commun.* **185** 2309–10
[174] Marzari N and Vanderbilt D 1997 *Phys. Rev.* B **56** 12847–65
[175] Souza I, Marzari N and Vanderbilt D 2002 *Phys. Rev.* B **65** 035109
[176] Poncé S, Margine E R, Verdi C and Giustino F 2016 *Comput. Phys. Commun.* **209** 116–33
[177] Filip M R, Volonakis G and Giustino F 2020 *Handbook of Materials Modeling: Applications: Current and Emerging Materials* (Springer International Publishing) pp 295–324
[178] Tao S, Schmidt I, Brocks G, Jiang J, Tranca I, Meerholz K and Olthof S 2019 *Nat. Commun.* **10** 2560
[179] Filip M R, Eperon G E, Snaith H J and Giustino F 2014 *Nat. Commun.* **5** 5757
[180] Even J, Pedesseau L, Jancu J M and Katan C 2013 *J. Phys. Chem. Lett.* **4** 2999
[181] Even J, Pedesseau L, Jancu J M and Katan C 2014 *Phys. Status Solidi RRL* **8** 31–35
[182] Rashba E I 1960 *Sov. Phys. Solid State* **2** 1109–22 (available at: www.webofscience.com/wos/woscc/full-record/WOS:A1960WT33500031)
[183] Dresselhaus G 1955 *Phys. Rev.* B **100** 580–6
[184] Zheng F, Tan L Z, Liu S and Rappe A M 2015 *Nano Lett.* **15** 7794–800
[185] Leppert L, Reyes-Lillo S E and Neaton J B 2016 *J. Phys. Chem. Lett.* **7** 3683–9
[186] Etienne T, Mosconi E and De Angelis F 2016 *J. Phys. Chem. Lett.* **7** 1638–45
[187] Etienne T, Mosconi E and De Angelis F 2018 *J. Phys. Chem.* C **122** 124–32
[188] Schlipf M and Giustino F 2021 *Phys. Rev. Lett.* **127** 237601
[189] Zhang X, Shen J-X, Wang W and Van de Walle C G 2018 *ACS Energy Lett.* **3** 2329–34
[190] Mosconi E, Amat A, Nazeeruddin M K, Grätzel M and De Angelis F 2013 *J. Phys. Chem.* C **117** 13902–13
[191] Umari P, Mosconi E and De Angelis F 2014 *Sci. Rep.* **4** 4467
[192] Burschka J, Pellet N, Moon S J, Humphry-Baker R, Gao P, Nazeeruddin M K and Grätzel M 2013 *Nature* **499** 316
[193] Stoumpos C C, Malliakas C D and Kanatzidis M G 2013 *Inorg. Chem.* **52** 9019–38
[194] Baikie T, Fang Y, Kadro J M, Schreyer M, Wei F, Mhaisalkar S G, Gratzel M and White T J 2013 *J. Mater. Chem.* A **1** 5628
[195] Fabini D H, Siaw T A, Stoumpos C C, Laurita G, Olds D, Page K, Hu J G, Kanatzidis M G, Han S and Seshadri R 2017 *J. Am. Chem. Soc.* **139** 16875–84
[196] Egger D A and Kronik L 2014 *J. Phys. Chem. Lett.* **5** 2728–33
[197] Bokdam M, Lahnsteiner J, Ramberger B, Schäfer T and Kresse G 2017 *Phys. Rev. Lett.* **119** 145504
[198] Menéndez-Proupin E, Palacios P, Wahnón P and Conesa J C 2014 *Phys. Rev.* B **90** 045207
[199] Scherpelz P, Govoni M, Hamada I and Galli G 2016 *J. Chem. Theor. Comput.* **12** 3523–44
[200] Poncé S, Schlipf M and Giustino F 2019 *ACS Energy Lett.* **4** 456–63
[201] Mosconi E, Umari P and De Angelis F 2016 *Phys. Chem. Chem. Phys.* **18** 27158–64
[202] Brivio F, Butler K T, Walsh A and van Schilfgaarde M 2014 *Phys. Rev.* B **89** 155204
[203] Ahmed T, La-o-vorakiat C, Salim T, Lam Y M, Chia E E M and Zhu J X 2015 *Europhys. Lett.* **108** 67015
[204] Troullier N and Martins J L 1991 *Phys. Rev.* B **43** 1993
[205] Blöchl P E 1994 *Phys. Rev.* B **50** 17953–79
[206] Vanderbilt D 1990 *Phys. Rev.* B **41** 7892
[207] Louie S G, Froyen S and Cohen M L 1982 *Phys. Rev.* B **26** 1738
[208] Hamann D R 2013 *Phys. Rev.* B **88** 085117
[209] Schlipf M and Gygi F 2015 *Comput. Phys. Commun.* **196** 36–44
[210] Heyd J, Scuseria G E and Ernzerhof M 2003 *J. Chem. Phys.* **118** 8207–15
[211] Bischoff T, Wiktor J, Chen W and Pasquarello A 2019 *Phys. Rev. Mater.* **3** 123802
[212] Blase X, Attaccalite C and Olevano V 2011 *Phys. Rev.* B **83** 115103
[213] Filip M R, Verdi C and Giustino F 2015 *J. Phys. Chem.* C **119** 25209–19
[214] Hybertsen M and Louie S 1987 *Comments Condend. Matter. Phys.* **13** 223–47
[215] Giustino F, Louie S G and Cohen M L 2010 *Phys. Rev. Lett.* **105** 265501
[216] Saidi W A, Poncé S and Monserrat B 2016 *J. Phys. Chem. Lett.* **7** 5247–52
[217] Zhao X-G, Wang Z, Malyi O I and Zunger A 2021 *Mater. Today* **49** 107–22
[218] Pan M, Li D, Fan J and Huang H 2022 *npj Comput. Mater.* **8** 1–13
[219] Seidl S A, Zhu X, Reuveni G, Aharon S, Gehrmann C, Caicedo-Dávila S, Yaffe O and Egger D A 2023 *Phys. Rev. Mater.* **7** L092401

[220] Sutton R J, Filip M R, Haghighirad A A, Sakai N, Wenger B, Giustino F and Snaith H J 2018 *ACS Energy Lett.* **3** 1787–94
[221] Zacharias M and Giustino F 2020 *Phys. Rev. Res.* **2** 013357
[222] Zacharias M, Volonakis G, Giustino F and Even J 2023 *Phys. Rev.* B **108** 035155
[223] Athinarayanarao D, Prod'hon R, Chamoret D, Qi J, Bodaghi M, André J-C and Demoly F 2023 *npj Comput. Mater.* **9** 1–13
[224] D'Innocenzo V, Grancini G, Alcocer M J P, Kandada A R S, Stranks S D, Lee M M, Lanzani G, Snaith H J and Petrozza A 2014 *Nat. Commun.* **5** 3586
[225] Miyata A, Mitioglu A, Plochocka P, Portugall O, Wang J T-W, Stranks S D, Snaith H J and Nicholas R J 2015 *Nat. Phys.* **11** 582–7
[226] Singh S, Li C, Panzer F, Narasimhan K L, Graeser A, Gujar T P, Köhler A, Thelakkat M, Huettner S and Kabra D 2016 *J. Phys. Chem. Lett.* **7** 3014–21
[227] Davies C L, Filip M R, Patel J B, Crothers T W, Verdi C, Wright A D, Milot R L, Giustino F, Johnston M B and Herz L M 2018 *Nat. Commun.* **9** 293
[228] Elliott R J 1957 *Phys. Rev.* **108** 1384–9
[229] Saba M *et al* 2014 *Nat. Commun.* **5** 5049
[230] Herz L M 2018 *J. Phys. Chem. Lett.* **9** 6853–63
[231] Heidrich K, Künzel H and Treusch J 1978 *Solid State Commun.* **25** 887–9
[232] Galkowski K *et al* 2016 *Energy Environ. Sci.* **9** 962–70
[233] a Pérez-Osorio M, Milot R L, Filip M R, Patel J B, Herz L M, Johnston M B and Giustino F 2015 *J. Phys. Chem.* C **119** 25703–18
[234] Sun J, Yang J and Ullrich C A 2020 *Phys. Rev. Res.* **2** 013091
[235] Cappellini G, Del Sole R, Reining L and Bechstedt F 1993 *Phys. Rev.* B **47** 9892–5
[236] Da Jornada F H, Qiu D Y and Louie S G 2017 *Phys. Rev.* B **95** 035109
[237] Alvertis A M, Champagne A, Del Ben M, da Jornada F, Qiu D Y, Filip M R and Neaton J B 2023 *Phys. Rev.* B **108** 235117
[238] Dai Z, Lian C, Lafuente-Bartolome J and Giustino F 2024 *Phys. Rev. Lett.* **132** 036902
[239] Dai Z, Lian C, Lafuente-Bartolome J and Giustino F 2024 *Phys. Rev.* B **109** 045202
[240] Bai Y, Wang Y and Meng S 2023 arXiv:2311.12662
[241] Mahanti S D and Varma C M 1970 *Phys. Rev. Lett.* **25** 1115–9
[242] Mahanti S D and Varma C M 1972 *Phys. Rev.* B **6** 2209–26
[243] Pollmann J and Büttner H 1977 *Phys. Rev.* B **16** 4480–90
[244] Kane E O 1978 *Phys. Rev.* B **18** 6849–55
[245] Wright A D, Verdi C, Milot R L, Eperon G E, Pérez-Osorio M, Snaith H J, Giustino F, Johnston M B and Herz L M 2016 *Nat. Commun.* **7** 11755
[246] Milot R L, Eperon G E, Snaith H J, Johnston M B and Herz L M 2015 *Adv. Funct. Mater.* **25** 6218–27
[247] Baranowski M and Plochocka P 2020 *Adv. Energy Mater.* **10** 1903659
[248] Buizza L R V and Herz L M 2021 *Adv. Mater.* **33** 2007057
[249] Fröhlich H 1954 *Adv. Phys.* **3** 325–61
[250] Chen Y, Motti S G, Oliver R D J, Wright A D, Snaith H J, Johnston M B, Herz L M and Filip M R 2022 *J. Phys. Chem. Lett.* **13** 4184–92
[251] Kokott S, Levchenko S V, Rinke P and Scheffler M 2018 *New J. Phys.* **20** 033023
[252] Sio W H, Verdi C, Poncé S and Giustino F 2019 *Phys. Rev.* B **99** 235139
[253] Sio W H, Verdi C, Poncé S and Giustino F 2019 *Phys. Rev. Lett.* **122** 246403
[254] Schlipf M, Poncé S and Giustino F 2018 *Phys. Rev. Lett.* **121** 086402
[255] Feynman R P 1955 *Phys. Rev.* **97** 660–5
[256] Miyata K, Meggiolaro D, Trinh M T, Joshi P P, Mosconi E M, Jones S C, De Angelis F and Zhu X-Y 2017 *Sci. Adv.* **3** e1701217
[257] Ambrosio F, Wiktor J, Angelis F D and Pasquarello A 2018 *Energy Environ. Sci.* **11** 101–5
[258] Schilcher M J, Abramovitch D J, Mayers M Z, Tan L Z, Reichman D R and Egger D A 2023 *Phys. Rev. Materials* **7** L081601
[259] Neukirch A J *et al* 2016 *Nano Lett.* **16** 3809–16
[260] Österbacka N, Erhart P, Falletta S, Pasquarello A and Wiktor J 2020 *Chem. Mater.* **32** 8393–400
[261] Ghosh D, Welch E, Neukirch A J, Zakhidov A and Tretiak S 2020 *J. Phys. Chem. Lett.* **11** 3271–86
[262] Saliba M *et al* 2016 *Science* **354** 206–9
[263] Saliba M *et al* 2016 *Energy Environ. Sci.* **9** 1989–97
[264] Yi C, Luo J, Meloni S, Boziki A, Ashari-Astani N, Grätzel C, Zakeeruddin S M, Röthlisberger U and Grätzel M 2016 *Energy Environmental Science* **9** 656–62
[265] Lee J-W, Kim D-H, Kim H-S, Seo S-W, Cho S M and Park N-G 2015 *Adv. Energy Mater.* **5** 1501310
[266] McMeekin D P *et al* 2016 *Science* **351** 151–5
[267] Bush K A *et al* 2017 *Nat. Energy* **2** 17009
[268] Eperon G E *et al* 2016 *Science* **354** 861–5
[269] Larach S, Shrader R E and Stocker C F 1957 *Phys. Rev.* **108** 587–9
[270] Savill K J, Ulatowski A M and Herz L M 2021 *ACS Energy Lett.* **6** 2413–26
[271] Hao F, Stoumpos C C, Cao D H, Chang R P H and Kanatzidis M G 2014 *Nat. Phot.* **8** 489–94
[272] Noh J H, Im S H, Heo J H, Mandal T N and Seok S I 2013 *Nano Lett.* **13** 1764–9
[273] Brennan M C, Draguta S, Kamat P V and Kuno M 2018 *ACS Energy Lett.* **3** 204–13
[274] Beal R E, Slotcavage D J, Leijtens T, Bowring A R, Belisle R A, Nguyen W H, Burkhard G F, Hoke E T and McGehee M D 2016 *J. Phys. Chem. Lett.* **7** 746–51
[275] Eperon G E, Stranks S D, Menelaou C, Johnston M B, Herz L M and Snaith H J 2014 *Energy Environ. Sci.* **7** 982–8
[276] Saffari M, Mohebpour M A, Soleimani H R and Tagani M B 2017 *J. Phys. D: Appl. Phys.* **50** 415501
[277] Colella S *et al* 2013 *Chem. Mater.* **25** 4613–8
[278] Kim J, Lee S-H, Chung C-H and Hong K-H 2016 *Phys. Chem. Chem. Phys.* **18** 4423–8
[279] Ornelas-Cruz I, Trejo A, Oviedo-Roa R, Salazar F, Carvajal E, Miranda A and Cruz-Irisson M 2020 *Comput. Mater. Sci.* **178** 109619
[280] Fykouras K, Lahnsteiner J, Leupold N, Tinnemans P, Moos R, Panzer F, de Wijs G A, Bokdam M, Grüninger H and Kentgens M 2023 *J. Mater. Chem.* A **11** 4587–97
[281] Bellaiche L and Vanderbilt D 2000 *Phys. Rev.* B **61** 7877–82
[282] Jong U G, Yu C J, Ri J S, Kim N H and Ri G C 2016 *Phys. Rev.* B **94** 125139
[283] Yu C-J, Ko U-H, Hwang S-G, Kim Y-S, Jong U-G, Kye Y-H and Ri C-H 2020 *Phys. Rev. Mater.* **4** 045402

[284] Drisdell W S *et al* 2017 *ACS Energy Lett.* **2** 1183–9
[285] Ferdani D W, Pering S R, Ghosh D, Kubiak P, Walker A B, Lewis S E, Johnson A L, Baker P J, Islam M S and Cameron P J 2019 *Energy Environ. Sci.* **12** 2264–72
[286] Ghosh D, Smith A R, Walker A B and Islam M S 2018 *Chem. Mater.* **30** 5194–204
[287] Slavney A H, Hu T, Lindenberg A M and Karunadasa H I 2016 *J. Am. Chem. Soc.* **138** 2138–41
[288] McClure E T, Ball M R, Windl W and Woodward P M 2016 *Chem. Mater* **6** 1348–54
[289] Volonakis G, Filip M R, Haghighirad A A, Sakai N, Wenger B, Snaith H J and Giustino F 2016 *J. Phys. Chem. Lett.* **7** 1254–9
[290] Filip M R, Hillman S, Haghighirad A A, Snaith H J and Giustino F 2016 *J. Phys. Chem. Lett.* **7** 2579–85
[291] Volonakis G, Haghighirad A A, Milot R L, Sio W H, Filip M R, Wenger B, Johnston M B, Herz L M, Snaith H J and Giustino F 2017 *J. Phys. Chem. Lett.* **8** 772–8
[292] Slavney A H, Leppert L, Saldivar Valdes A, Bartesaghi D, Savenije T J, Neaton J B and Karunadasa H I 2018 *Ang. Chem. Int. Ed.* **57** 12765–70
[293] Lee B, Stoumpos C C, Zhou N, Hao F, Malliakas C, Yeh C-Y, Marks T J, Kanatzidis M G and Chang R P H 2014 *J. Am. Chem. Soc.* **136** 15379–85
[294] Sakai N, Haghighirad A A, Filip M R, Nayak P K, Nayak S, Ramadan A, Wang Z, Giustino F and Snaith H J 2017 *J. Am. Chem. Soc.* **139** 6030–3
[295] Slavney A H, Connor B A, Leppert L and Karunadasa H I 2019 *Chem. Sci.* **10** 11041
[296] Biega R I, Filip M R, Leppert L and Neaton J B 2021 *J. Phys. Chem. Lett.* **12** 2057–63
[297] Maughan A E, Ganose A M, Bordelon M M, Miller E M, Scanlon D O and Neilson J R 2016 *J. Am. Chem. Soc.* **138** 8453–64
[298] Longo G, Mahesh S, Buizza L R V, Wright A D, Ramadan A J, Abdi-Jalebi M, Nayak P K, Herz L M and Snaith H J 2020 *ACS Energy Lett.* **5** 2200–7
[299] Palummo M, Berrios E, Varsano D and Giorgi G 2020 *ACS Energy Lett.* **5** 457–63
[300] Biega R I, Chen Y, Filip M R and Leppert L 2023 *Nano Lett.* **23** 8155–61
[301] Leppert L 2024 *J. Chem. Phys.* **160** 050902
[302] Luo J *et al* 2018 *Nature* **563** 541–5
[303] Meng W, Wang X, Xiao Z, Wang J, Mitzi D B and Yan Y 2017 *J. Phys. Chem. Lett.* **8** 2999–3007
[304] Slavney A H, Leppert L, Bartesaghi D, Gold-Parker A, Toney M F, Savenije T J, Neaton J B and Karunadasa H I 2017 *J. Am. Chem. Soc.* **139** 5015–8
[305] Lindquist K P, Mack S A, Slavney A H, Leppert L, Gold-Parker A, Stebbins J F, Salleo A, Toney M F, Neaton J B and Karunadasa H I 2019 *Chem. Sci.* **10** 10620
[306] Liao Q, Chen J, Zhou L, Wei T, Zhang L, Chen D, Huang F, Pang Q and Zhang J Z 2020 *J. Phys. Chem. Lett.* **11** 8392–8
[307] Klarbring J, Singh U, Simak S I and Abrikosov I A 2023 *Phys. Rev. Mater.* **7** 044605
[308] Jöbsis H J, Fykouras K, Reinders J W, van Katwijk J, Dorresteijn J M, Arens T, Vollmer I, Muscarella L A, Leppert L and Hutter E M 2023 *Adv. Funct. Mater.* 2306106
[309] Singh U, Klarbring J, Abrikosov I A and Simak S I 2023 *Phys. Rev. Mater.* **7** 114404
[310] Zelewski S J *et al* 2019 *J. Mater. Chem.* C **7** 8350–6
[311] Wright A D, Buizza L R V, Savill K J, Longo G, Snaith H J, Johnston M B and Herz L M 2021 *J. Phys. Chem. Lett.* **12** 3352–60
[312] Baskurt M and Wiktor J 2023 *J. Phys. Chem.* C **127** 23966–72
[313] Ha V A, Volonakis G, Lee H, Zacharias M and Giustino F 2021 *J. Phys. Chem.* C **125** 21689–700
[314] Du K Z, Meng W, Wang X, Yan Y and Mitzi D B 2017 *Angew. Chem. Int. Ed.* **56** 8158–62
[315] Hong X, Ishihara T and Nurmikko A V 1992 *Phys. Rev.* B **45** 6961–4
[316] Cheng B *et al* 2018 *Commun. Phys.* **1** 80
[317] Leveille J, Katan C, Zhou L, Mohite A D, Even J, Tretiak S, Schleife A and Neukirch A J 2018 *Phys. Rev. Mater.* **2** 105406
[318] Leveillee J, Katan C, Even J, Ghosh D, Nie W, Mohite A D, Tretiak S, Schleife A and Neukirch A J 2019 *Nano Lett.* **19** 8732–40
[319] Passarelli J V *et al* 2020 *Nat. Chem.* **12** 672–82
[320] McArthur J, Filip M R and Qiu D Y 2023 *Nano Lett.* **23** 3796–802
[321] Biega R I, Bokdam M, Herrmann K, Mohanraj J, Skrybeck D, Thelakkat M, Retsch M and Leppert L 2023 *J. Phys. Chem.* C **127** 9183–95
[322] Marchenko E I, Korolev V V, Fateev S A, Mitrofanov A, Eremin N N, Goodilin E A and Tarasov A B 2021 *Chem. Mater.* **33** 7518–26
[323] Knutson J L, Martin J D and Mitzi D B 2005 *Inorg. Chem.* **44** 4699–705
[324] Dyksik M *et al* 2020 *ACS Energy Lett.* **5** 3609–16
[325] Kamminga M E, de Wijs G A, Havenith R W A, Blake G R and Palstra T T 2017 *Inorg. Chem.* **56** 8408–14
[326] Connor B A, Su A C, Slavney A H, Leppert L and Karunadasa H I 2023 *Chem. Sci.* **14** 11858–71
[327] Cho Y, Greene S M and Berkelbach T C 2021 *Phys. Rev. Lett.* **126** 216402
[328] Blancon J C *et al* 2018 *Nat. Commun.* **9** 2254
[329] Cho Y and Berkelbach T C 2019 *J. Phys. Chem. Lett.* **10** 6189–96
[330] Molina-Sánchez A 2018 *ACS Appl. Energy Mater.* **1** 6361–7
[331] Filip M R, Qiu D Y, Del Ben M and Neaton J B 2022 *Nano Lett.* **22** 4870–8
[332] Chen Y and Filip M R 2023 *J. Phys. Chem. Lett.* **14** 10634–41
[333] Boeije Y *et al* 2023 *J. Am. Chem. Soc.* **145** 21330–43
[334] Forde A, Tretiak S and Neukirch A J 2023 *Nano Lett.* **23** 11586–92
[335] Pantaler M *et al* 2022 *JACS Au* **2** 136–49
[336] Del Ben M, da Jornada F H, Canning A, Wichmann N, Raman K, Sasanka R, Yang C, Louie S G and Deslippe J 2019 *Comput. Phys. Commun.* **235** 187–95
[337] Ben M D, Yang C, Li Z, da Jornada F H, Louie S G and Deslippe J 2020 Accelerating large-scale excited-state GW calculations on leadership HPC systems *SC20: Int. Conf. for High Performance Computing, Networking, Storage and Analysis* pp 1–11
[338] Aubrey M L, Saldivar Valdes A, Filip M R, Connor B A, Lindquist K P, Neaton J B and Karunadasa H I 2021 *Nature* **597** 355–9
[339] Rieger S *et al* 2019 *Phys. Rev.* B **100** 201404
[340] Freysoldt C, Grabowski B, Hickel T, Neugebauer J, Kresse G, Janotti A and Van De Walle C G 2014 *Rev. Mod. Phys.* **86** 253–305
[341] Meggiolaro D and De Angelis F 2018 *ACS Energy Lett.* **3** 2206–22
[342] Whalley L D, Skelton J M, Frost J M and Walsh A 2016 *Phys. Rev.* B **94** 220301(R)
[343] Gehrmann C and Egger D A 2019 *Nat. Commun.* **10** 3141

[344] Menahem M, Dai Z, Aharon S, Sharma R, Asher M, Diskin-Posner Y, Korobko R, Rappe A M and Yaffe O 2021 *ACS Nano* **15** 10153–62
[345] Lahnsteiner J and Bokdam M 2022 *Phys. Rev.* B **105** 024302
[346] Cohen A V, Egger D A, Rappe A M and Kronik L 2019 *J. Phys. Chem. Lett.* **10** 4490–8
[347] Refaely-Abramson S, Qiu D Y, Louie S G and Neaton J B 2018 *Phys. Rev. Lett.* **121** 167402
[348] Lewis D K and Sharifzadeh S 2019 *Phys. Rev. Mater.* **3** 114601
[349] Sun Q and Chan G K-L 2016 *Acc. Chem. Res.* **49** 2705–12
[350] Wasserman A and Pavanello M 2020 *Int. J. Quantum Chem.* **120** e26495
[351] Vorwerk C, Sheng N, Govoni M, Huang B and Galli G 2022 *Nat. Comput. Sci.* **2** 424–32
[352] Westermayr J and Marquetand P 2021 *Chem. Rev.* **121** 9873–926
[353] Jiang Y, Stull S L, Shao Q and Yang Z J 2022 *Electron. Struct.* **4** 044007
[354] Teale A M *et al* 2022 *Phys. Chem. Chem. Phys.* **24** 28700–81
[355] Govoni M and Galli G 2015 *J. Chem. Theo. Comput.* **11** 2680–96
[356] Förster A and Visscher L 2020 *J. Chem. Theor. Comput.* **16** 7381–99
[357] Wilhelm J, Seewald P and Golze D 2021 *J. Chem. Theor. Comput.* **17** 1662–77